# Multiple protein-protein interactions drive the assembly and budding of the Chikungunya virion.

*Miguel Angel Coronado-Ipiña[1,2,#], Shuyang Zhang[3,#], Siyu Li[3++], Pedro Gerardo Hernández-Sánchez[1], Denisse Cadena-Lopez[1,2,+], Vanessa Labrada-Martagón[5], Suchetana Mukhopadyay[6], Roya Zandi[3*], Mauricio Comas-Garcia[1,4,5,*]*

[1]High-Resolution Microscopy Section, Research Center for Health Sciences and Biomedicine, Autonomous University of San Luis Potosi, Mexico

[2]Life Sciences Graduate Program, Department of Sciences, Autonomous University of San Luis Potosi, Mexico

[3]Department of Physics, University of California, Riverside

[4]Molecular and Translational Medicine Section, Research Center for Health Sciences and Biomedicine, Autonomous University of San Luis Potosi, Mexico

[5]Department of Sciences, Autonomous University of San Luis Potosi, Mexico

[6]Department of Biology, Indiana University Bloomington

+ Current address: ThermoFisher Mexico

++ Current address: Department of Physics and Astronomy, California State Polytechnic University, Pomona, California 91768, USA.

*Correspondence: royaz@ucr.edu and mauricio.comas@uaslp.mx

#These two authors contribute equally

## ABSTRACT

The assembly of enveloped viruses is a highly orchestrated process that depends on the coupling of multiple protein–protein interactions within a membrane environment. To gain mechanistic insight into this process, we use Chikungunya virus as a model system to study Alphavirus

assembly, focusing on the interplay between core–spike and spike–spike interactions. We begin with coarse-grained molecular dynamics simulations to systematically explore how the symmetry of the nucleocapsid core, together with the relative strengths of spike–core and spike–spike interactions, influences budding efficiency and the emergence of icosahedral particle symmetry. Building on these computational predictions, we perform site-directed mutagenesis on Chikungunya virus 181/25 and examine the consequences for particle assembly and budding in cultured cells, as well as the impact of these mutations during *in-cellulo* assembly. Our results reveal that canonical core–spike interactions, while necessary, are not sufficient for successful assembly. Instead, lateral interactions among glycoproteins emerge as critical determinants of efficient budding, particle stability, and the maintenance of icosahedral symmetry. Together, these findings provide an integrated computational and experimental framework for understanding the molecular principles governing Alphavirus assembly.

**KEYWORDS:** Enveloped virion budding, glycoprotein steric repulsions, Alphaviruses, Molecular Dynamics simulations, multiple protein interactions

The assembly of enveloped viruses is a complex, highly regulated process that involves orchestrated protein–protein and protein–membrane interactions to drive membrane deformation, budding, and packaging of the viral genome into a fully infectious particle[1-7]. For certain viruses, such as retroviruses and filoviruses, this process is relatively well understood. It is known to rely primarily on matrix or capsid proteins that recruit host-cell machinery to mediate budding from the plasma membrane [6, 8-13]. In contrast, the mechanisms of assembly and budding in Alphaviruses

46 remain less well characterized, with a number of, and at times conflicting, models proposed over
47 the past two decades[2, 14-18].

48 *Alphaviruses* are a genus of Arthropod-borne viruses that infect a wide range of animals;
49 these viruses can be grouped as either New- or Old-World Alphaviruses, depending on whether
50 they are endemic to the American continent or elsewhere, respectively [19]. With a few exceptions,
51 members of these two groups are phylogenetically related. Chikungunya virus (CHIKV), a
52 mosquito-borne Old-World Alphavirus, is the most prevalent Alphavirus infecting humans and
53 has caused recurrent epidemics of febrile illness and chronic polyarthritis worldwide[20-25]. All
54 Alphaviruses share a conserved spherical virion architecture approximately 70 nm in diameter,
55 consisting of two concentric icosahedral protein shells separated by a lipid bilayer derived from
56 the host plasma membrane. The outer shell comprises 240 copies of E1–E2 heterodimers arranged
57 as 80 trimeric spikes, while the inner shell, nucleocapsid or core (NC), consists of 240 capsid
58 proteins (CP) encapsidating the ~12 kb single-stranded positive-sense RNA genome[14]. These two
59 layers are structurally coupled via interactions between the cytoplasmic tail of E2 and a
60 hydrophobic pocket in the capsid protein[14, 26].

61 Cryo-electron microscopy (cryo-EM), cryo-electron tomography (cryo-ET), biochemical
62 analysis, and molecular dynamics simulation studies of Alphaviruses have revealed four major
63 classes of interactions stabilizing the virion: (1) intra-dimer interactions[3, 4], (2) inter-dimer E1–
64 E2[2, 16, 27-29] , (3) inter-spike trimer–trimer interactions[30, 31], and (4) vertical contacts between E2
65 and the capsid core[26, 30, 32-34]. These interactions are thought to orchestrate every stage of virion
66 formation, from initiating budding and guiding icosahedral assembly to determining the efficiency

67 of particle production, the structural stability of the virion, and ultimately its infectivity[14, 35, 36], yet
68 the precise roles and mechanistic impact of each contact remain incompletely understood.

69 A central question in Alphavirus biology is how these two icosahedral layers assemble in
70 a coordinated manner during virus budding. Several models have been proposed: in the assembly-
71 from-within model, a preformed icosahedral core serves as a structural template for glycoprotein
72 assembly [15, 17]; in the assembly-from-without model, glycoproteins initiate budding and recruit the
73 capsid core *post hoc*[16]; and in the concerted assembly model, an initially irregular cytoplasmic core
74 gains order upon interacting with glycoproteins at the membrane[2, 18]. The latter has gained support
75 from recent cryo-ET studies, which show that alphavirus cores lack icosahedral symmetry in the
76 cytoplasm but acquire structural order at the plasma membrane through interactions with spikes [2,
77 18]. Notably, these studies did not observe a pre-assembled lattice of spikes at the membrane or
78 icosahedral cytoplasmic cores, suggesting that E2–core binding and lateral glycoprotein
79 interactions drive budding and shape the geometry of the final virion. However, in the absence of
80 direct, molecular-resolution visualization of both the budding process and spike organization under
81 budding-inhibited conditions in infected cells, the mechanisms underlying icosahedral assembly
82 and its inhibition remain poorly defined.

83 To understand the factors contributing to the budding of alphaviruses such as Sindbis,
84 Hagan and co-workers developed a coarse-grained simulation model that incorporates spike–spike
85 and spike–core interactions[30]. They showed that while glycoprotein interactions alone can drive
86 budding, the resulting particles tend to be polydisperse and irregular. Including even modest
87 interactions with a rigid core improves uniformity and reduces kinetic trapping. However, their

88 focus was on the conditions that permit or impede budding, rather than on achieving icosahedral
89 symmetry in the final product.

90 Here, we investigate the molecular determinants of Chikungunya virus (CHIKV) budding
91 and assembly by identifying the specific interactions that govern these processes. A central
92 unresolved question is whether capsid proteins (CPs) pre-assemble into icosahedral NCs that serve
93 as structural templates, or whether glycoprotein spikes instead drive the coordinated assembly of
94 the outer spike lattice and the inner NC shell. To address this, we used coarse-grained molecular
95 dynamics simulations to systematically investigate how the symmetry of the core, along with
96 spike–core and spike–spike interactions, influences budding efficiency and the emergence of
97 icosahedral particle symmetry. We investigated whether immature, non-icosahedral NCs can
98 function as rough scaffolds that trigger the formation of icosahedral spike shells. Guided by our
99 simulation results, we carried out targeted mutational experiments using a CHIKV reporter virus
100 system to test the functional roles of key glycoprotein interfaces, including intradimer, intertrimer,
101 and spike–core contacts. To dissect the contributions of each interaction, we introduced three
102 specific mutations: E2 Y400K/L402R to disrupt spike–core interactions; E2 N263Q to impair
103 intertrimer contacts; and E1 K245N/R247T to weaken intradimer interactions. This integrated
104 computational and experimental approach enabled us to dissect the contributions of individual
105 interactions to efficient virion formation.

106 In our MD simulations, we find that if the core lacks icosahedral symmetry and is
107 constrained to a fixed geometry that cannot locally dissociate and reassociate, the spikes fail to
108 form a complete icosahedral shell. In contrast, if the core exhibits an imperfect icosahedral
109 structure, such as one missing an entire pentamer, spike assembly can still proceed toward

110 icosahedral symmetry, albeit with reduced efficiency. These findings strongly support a concerted
111 assembly model, in which tightly coordinated interactions across the membrane guide the
112 formation of both icosahedral layers.

113 Furthermore, our experimental results we show that E2–core interactions are critical for
114 initiating membrane curvature and nucleating particle formation. However, successful and
115 efficient assembly of structurally complete and infectious CHIKV virions also requires strong
116 lateral interactions between glycoprotein spikes. Disruption of either vertical (spike–core) or
117 lateral (spike–spike) interactions compromises assembly fidelity, reduces infectivity, or blocks
118 budding altogether. Our combined simulations and experiments demonstrate that both spike–core
119 interactions and lateral interactions among spikes play essential roles in establishing and
120 stabilizing icosahedral symmetry across the two structural layers of the virus. This cooperative
121 mechanism ensures proper virion architecture and function. It highlights key vulnerabilities that
122 could be targeted by antiviral strategies aimed at disrupting envelope protein organization and
123 blocking particle assembly or release.
124

125 **RESULTS AND DISCUSSION**

126 Motivated by several experiments on CHIKV budding and the formation of icosahedral symmetry,
127 carried out by Chiu's group [2, 18, 37] and others[27, 30, 38-40], we use coarse-grained molecular dynamics
128 simulations to systematically investigate how specific spike–spike and spike–core interactions
129 influence virus assembly. This computational framework enables us to isolate the roles of
130 individual interactions in a controlled environment, free from cellular complexity. The insights
131 gained from these simulations guided the design of targeted mutational experiments using CHIKV
132 181/25 with a reporter gene[41] to determine the role of these interactions in the assembly of viral

133 particles in cultured cells, establishing a direct connection between the physical interaction
134 parameters and their functional consequences in infected cells—results we present following the
135 simulation section.
136
137 **Molecular Dynamics Simulations**
138 We employed coarse-grained molecular dynamics simulations[42] to study the assembly and budding
139 processes of CHIKV under various scenarios. The model successfully demonstrates the effects of
140 spike–core interactions and spike–spike interactions between trimers during budding and
141 assembly. However, it does not account for the impact of altering the intradimer surface, which
142 modifies interactions between heterodimers within individual trimers, a level of detail beyond the
143 resolution of our current model.
144 We first optimize the system by tuning the spike–spike and spike–core interaction strengths
145 to identify conditions that support efficient budding. To establish these baseline parameters, we
146 simulated the budding of a plain spherical particle through the membrane, followed by the budding
147 of a preassembled icosahedral core. We then examined how altering the CTD-Core and trimer-
148 trimer interactions affects the assembly and budding processes. These MD simulations analyze the
149 impact of budding from both fully formed and imperfect icosahedral shells. These were validated
150 by infecting and transfecting HEK-293T cells with a CHIKV CMV-driven system expressing a
151 reporter gene.
152 While the primary focus of our work is on core–spike interactions and the role of the core
153 in guiding the icosahedral arrangement of spikes, we also investigated whether glycoprotein
154 interactions alone can drive budding in the absence of a core. Consistent with previous studies, our
155 results show that although spike–spike interactions are sufficient to initiate budding, the resulting

particles are often polydisperse and lack a regular structure [29, 30, 43, 44]. We observed that budding still occurs without a core if the lateral interactions between glycoprotein spikes are strong enough, though the resulting particles are often irregular and lack icosahedral symmetry.

In the following sections, we examine three classes of interactions between cores and spikes (see Figure 1). Specifically, our simulations focus on the interactions between the cytosolic C-terminal domains of the spikes and the core (CTD–core, $\varepsilon_{mc}$), the lateral interactions between the transmembrane domains of the spikes (TMD–TMD, $\varepsilon_{mm}$), and the excluded-volume interactions between the spike ectodomains (ED–ED). We first present our results for a plain spherical core, which provides a baseline for understanding the role of geometry. The analysis is then extended to an icosahedral core, allowing us to capture the effects of symmetry and structural constraints.

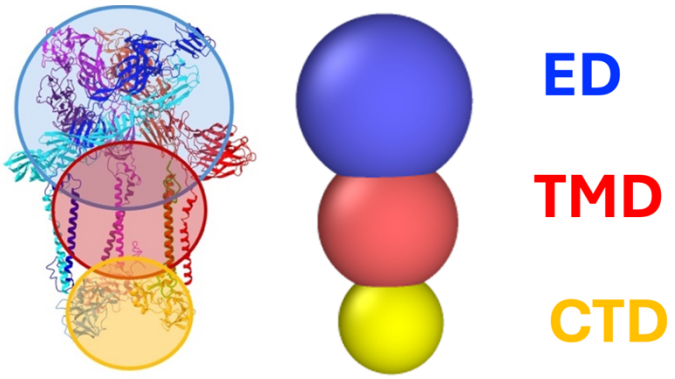


**Figure 1.** *Schematic representation of a coarse-grained spike protein.* The atomic structure of the CHIKV spike protein, a trimer of heterodimers, was obtained from the Protein Data Bank (PDB ID: 8FCG). The shaded circles represent the components of the coarse-grained model, which consists of three spherical particles: ED (ecto domain, blue), TMD (transmembrane domain, red), and CD (cytoplasmic domain, yellow). ED has the largest diameter, followed by TMD, with CTD being the smallest. The size asymmetry allows the spike proteins to assume a curved configuration.

**Budding of a Plain Spherical Particle Through the Membrane**

We begin by performing simulations using a plain spherical core, as described in Figure 2A. Interestingly, we observed particle budding even with this simple spherical core. Although the budding region did not exhibit perfect T = 4 icosahedral symmetry, the total number of incorporated spike proteins averaged around 79 across five simulation trials, remarkably close to the expected number of 80 for a correctly assembled T = 4 shell. This suggests that core size alone, even when commensurate with T = 4 geometry, is not sufficient to ensure correct icosahedral symmetry; in this minimal configuration, the spatial arrangement of the spikes deviates from the expected symmetry.

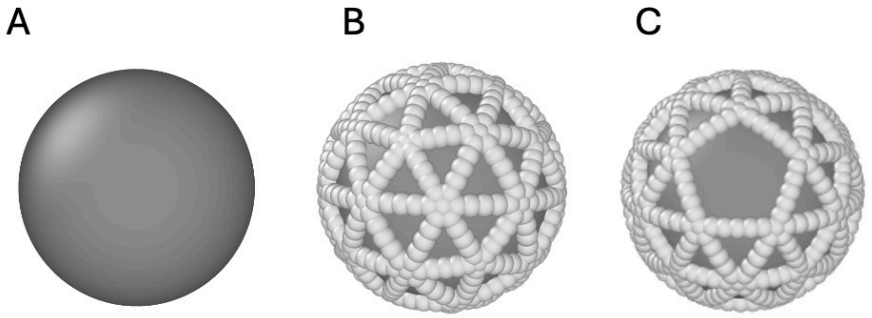


**Figure 2**. *Schematic view of core particles.* **A)** A simple spherical core. **B)** A spherical core decorated with 80 triangular units arranged with icosahedral symmetry. **C)** A modified version of core in which several triangles are missing, breaking the icosahedral symmetry.

All relevant interaction parameters, namely, the strength of the CTD–core interaction ($\varepsilon_{mc}$), the attractive interaction between TMD domains of neighboring spikes ($\varepsilon_{mm}$), and the excluded volume interactions, are provided in the caption of Figure 3. These parameters are optimized to

promote efficient budding, resulting in the core being decorated with ~80 spikes. We now turn to examine how the symmetry of the core influences the symmetry of the spike layer.

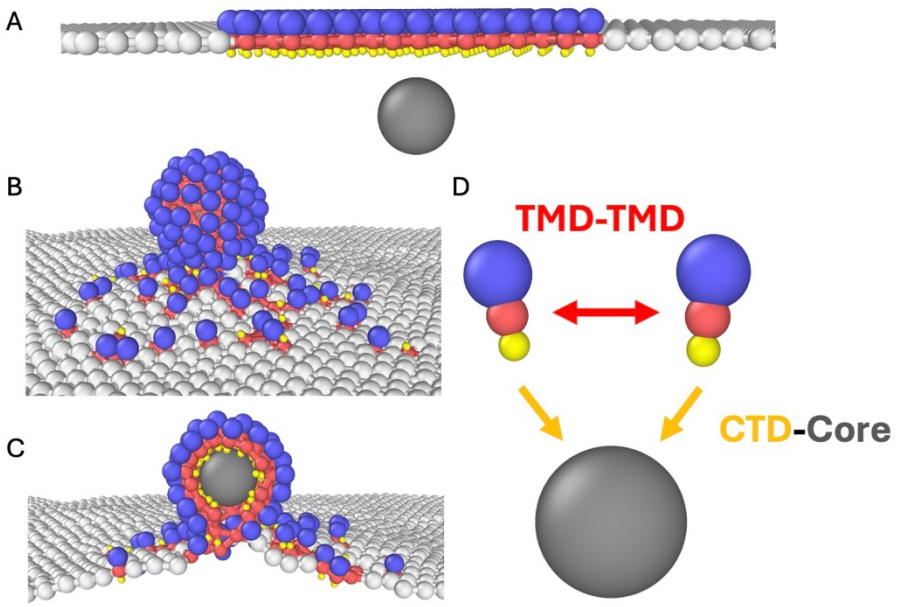


**Figure 3.** *Membrane and a plain spherical core.* **A)** The initial state of the system before budding. **B)** The final state of the system after budding. The final structure contains approximately 76–82 spikes but does not exhibit icosahedral symmetry. The system parameters include a CTD–core interaction strength of 25 $k_BT$ and a TMD-TMD interaction strength of 0. The particle diameters are set to 1.1 for ED, 0.8 for TMD, and 0.4 for CTD. **C)** The cross-sectional view of the final state after budding. **D)** Schematic representation of TMD-TMD and CTD-core interactions. Arrows indicate attractive interactions between TMD proteins and between CTD and the core. All other particles interact through steric interactions.

## Budding of an Icosahedral Core Through the Membrane

Instead of the plain spherical core used in the previous section, we now employ a core with icosahedral symmetry, as shown in Figure 2B. This core consists of 80 trimers arranged in a T=4 structure. When the CTD–core interaction is weak, the core fails to bud from the membrane,

consistent with previous studies[17, 26, 28, 32, 33]. We identified a critical interaction strength between the core and the CTDs of the spike proteins ($\varepsilon_{mc}$ =15 $k_BT$, see Eq. 3 and Supplementary Information). When $\varepsilon_{mc}$ falls below this threshold, the membrane remains undeformed despite the proximity of the core. This scenario captures the behavior of the mutant CT characterized in the experimental section below.

Figure 4A shows the initial configuration, where the core is placed near a membrane decorated with embedded spike proteins. As the simulation progresses, the attractive interaction ($\varepsilon_{mc}$ =15 $k_BT$) between the core and the CTDs drives membrane bending and initiates partial wrapping around the core. However, since the interaction strength is insufficient, budding halts prematurely, resulting in incomplete envelopment (Figure 4B). In these simulations, the attractive component of lateral spike–spike interactions was set to zero. The parameters used in these simulations are provided in the caption of Figure 4.

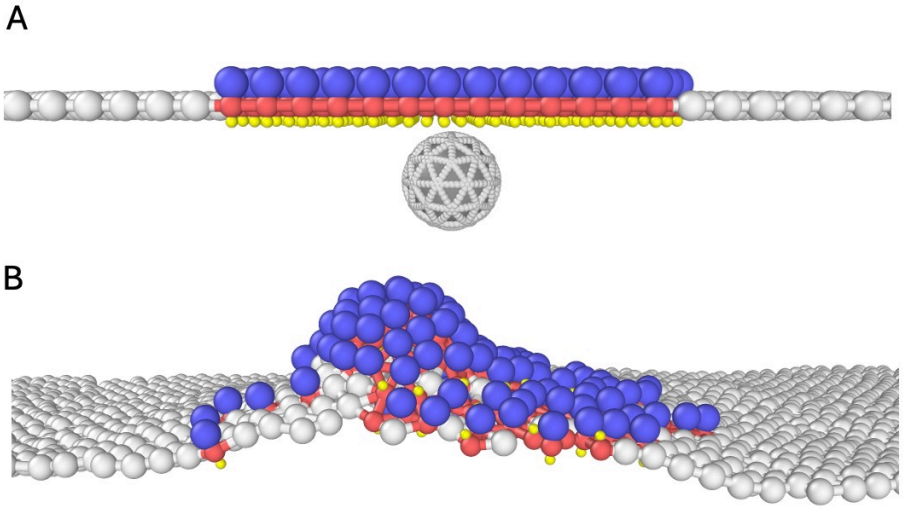


**Figure 4.** *Membrane and an icosahedral core.* **A)** Initial configuration of the system with a core exhibiting icosahedral symmetry**. B)** Final configuration after introducing a CTD–core interaction with strength ε = 15 $k_BT$. The core is stalled in this position. The TMD-TMD interaction strength is set to 0. The particle

diameters are set to 1.1 for ED, 0.8 for TMD, and 0.4 for CTD; all diameters are in units of a (see Eq.1). This structure is very similar to those we find by thin-section TEM when budding is arrested by introducing a mutation that alters the lateral interactions of the glycoproteins (see Figure 8B).

A substantially stronger CTD–core interaction, approximately 80 $k_BT$, is required to drive both complete budding and the emergence of icosahedral symmetry in the spike arrangement. The details underlying this value are provided in the Materials and Methods section. As previously mentioned, the model includes three key parameters: the strength of the interaction between the CTD of the spike proteins and the core ($\varepsilon_{mc}$), the attractive interaction between the TMD of neighboring spikes ($\varepsilon_{mm}$), and the excluded volume interactions (ED) among all other particles. Figure 5A shows snapshots from the simulation at an early budding stage, where an icosahedral core begins to deform the membrane and recruit spike proteins. As time progresses, more spikes attach to the core and begin to arrange in positions consistent with icosahedral symmetry. Figure 5B shows a later snapshot, corresponding to the end of the simulation. Although our model does not include a scission mechanism, budding proceeds until approximately 80±5 spike proteins are adsorbed onto the core, forming a nearly icosahedral structure. The parameters used in the simulation are provided in the figure caption. The inset in Figure 5B highlights the final configuration, with the positions of the attached spikes marked by small yellow spheres. A cutaway view in Figure 5C illustrates the spatial distribution of spikes around the core.

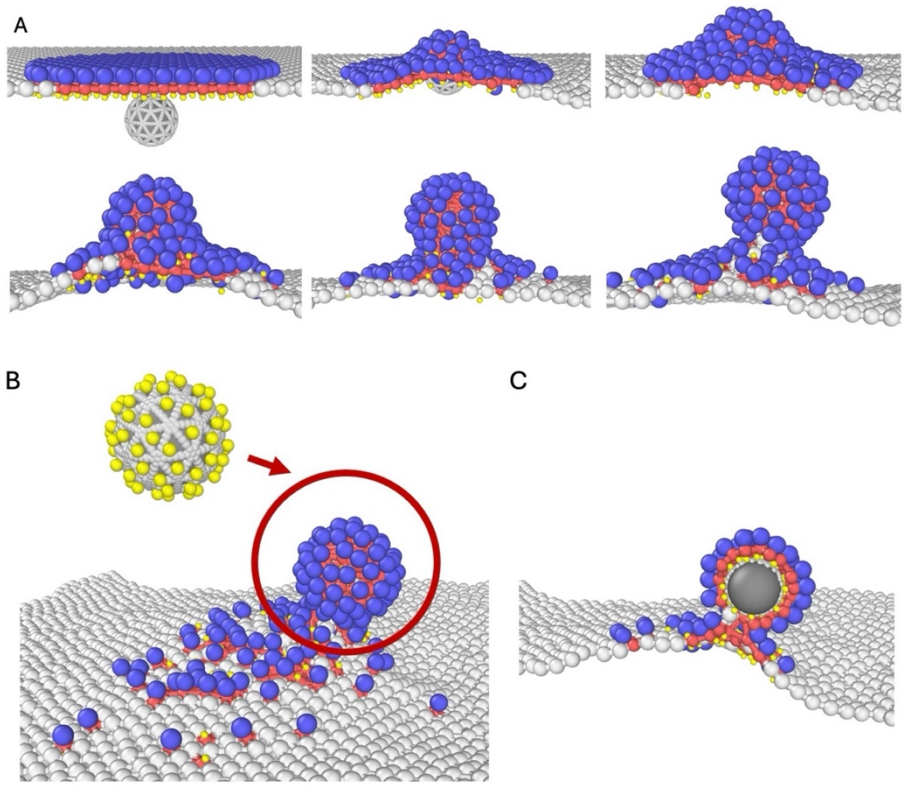


**Figure 5.** *Snapshots of the budding*. **A)** Snapshots of the budding process using an icosahedral core at timesteps t=0,5,10, 80,250, and 700 (left to right, top to bottom). **B)** Final state of the system after budding. The inset highlights the location of CTD particles along with the core. **C)** Final state shown in a vertical cross-sectional view sliced through the center. The system parameters include a CTD–core interaction strength of 80 $k_BT$. The particle diameters used in this simulation were: ED = 1.1, TMD = 0.8, and CTD = 0.4. The system includes LJ repulsion to account for excluded volume, but there are no attractive TMD-TMD interactions.

## Modeling the Effects of Mutations by Tuning Attractive and Steric Interactions Between Spike Protein Domains

Ribeiro-Filho et al. proposed that in the Mayaro virus, the glycosylation site equivalent to CHIKV E2 N263 acts as a "*molecular handshake*" that stabilizes the viral particles. This glycosylation site can easily influence trimer–trimer interactions through steric repulsion from the attached

carbohydrates. Its removal may also alter the local curvature or relative orientation between adjacent spikes, thereby making budding more difficult.

To quantify the effect of the absence of this glycosylation site in E2, we conducted a series of simulations with icosahedral cores and compared their relative success rates. We began by systematically varying all key parameters, ED size, TMD-TMD interaction strength, and CTD–core attraction, to identify the combination that produced the highest assembly efficiency. This optimal condition, corresponding to a CTD–core interaction strength of $\varepsilon_{mc} = 74\ k_BT$, along with default values for ED size and TMD-TMD attraction (specific values listed in Table 1), was designated as the wild-type (WT) baseline. Note that this value of $\varepsilon_{mc}$ results in an E2–core interaction strength of approximately 8 $k_BT$, consistent with previous studies (see Supplementary Information). To isolate the effects of specific mutations, we introduced changes by modifying one or more of these parameters, while holding the CTD–core interaction constant at $\varepsilon_{mc} = 74\ k_BT$. For each condition, we performed eight independent simulation trials. In the WT system ($\varepsilon_{mc} = 74\ k_BT$), 7 out of 8 simulations resulted in successful assemblies, which we define as a 100% baseline success rate. A configuration was considered successful if no more than five of the 80 spike proteins, expected in a perfect T=4 structure, were missing or mispositioned. This definition is consistent with recent Cryo-ET data that shows that Alphavirus budded virions can have defects in one pole of the particle[18].

**Table 1.** Simulation data on the Effects equivalent to mutant E2 N263.

| Icosahedral core (constant CTD-Core value) | Parameters | Successful rates | Percentage |
|---|---|---|---|
| WT | ED=1.15, CTD-Core=74, TMD-TMD=0.2 | 7/8 | 100.0% |
| Smaller ED | ED=1.1, CTD-Core=74, TMD-TMD=0.2 | 4/8 | 57.1% |
| No TMD-TMD | ED=1.15, CTD-Core=74 | 2/8 | 28.6% |
| No TMD-TMD + Smaller ED | ED=1.1, CTD-Core=74 | 1/8 | 14.39% |

For each set of parameters, we performed 8 independent simulation trials. "WT" refers to the wild-type system, which includes strong TMD-TMD interactions and an optimal ED size. The "TMD-TMD" and "CTD-Core" columns denote the interaction strengths (ε) used in the Lennard-Jones (LJ) potential. In different cases, we either reduced the ED size, removed the TMD-TMD interaction, or applied both modifications to assess their impact on the success rate. For all setups, the CTD–Core interaction strength was held constant at 74 $k_BT$. The success rate is defined as the ratio of successful budding events to the total number of trials. The final column presents the success rate as a percentage relative to the WT case. "ED size" refers to the diameter of the ED particle in units of *a*.

As shown in Table 1, reducing the ED size while keeping the CTD–core fixed at 74 $k_BT$ resulted in a drop in the success rate to approximately 57%. Eliminating the TMD–TMD interactions while maintaining the WT ED size also reduced the success rate to about 28.6%, highlighting the importance of attractive interactions between spike proteins. When both the ED size was reduced and the TMD–TMD interaction was removed, the success rate declined even further to 14.3%. These results suggest that decreasing ED size disrupts T = 4 formation, likely by impairing the induction of membrane curvature, and that the absence of TMD–TMD attraction further compromises proper assembly. Our findings indicate that both steric and attractive

interactions among spike proteins are essential for efficient and robust assembly. These simulations reflect the behavior of the mutant ITS described in the experimental section.

We next investigated how changes in the CTD–core interaction strength affect assembly outcomes in the mutated systems described above. Achieving the right balance is critical: an overly strong attraction can lead to excessive binding of spike proteins to the core, while a too weak interaction may fail to bring in enough spikes for successful assembly. To explore this, we performed additional simulations in which CTD–core strength was varied while holding the other parameters fixed at their mutated values. This allowed us to assess how changing the interaction strength affects budding efficiency under each mutation scenario.

Table 2 summarizes these findings. In the absence of TMD–TMD interaction, increasing CTD–core strength from 74 to 80 $k_BT$ improved the success rate to 85.7% relative to WT. When only the ED size was reduced and the CTD–core was set to 75, the success rate reached 71.4%. However, when both ED size was reduced and TMD–TMD interaction was removed, success fell again to 57.1%. Notably, while stronger CTD–core attraction improves assembly efficiency, it also results in excessive spike adsorption in the WT system, underscoring the importance of a finely tuned interplay among all interactions for successful T=4 structure formation.

**Table 2.** Data for the icosahedral core with varying CTD–Core interaction strength.

| Icosahedral core (optimal CTD-Core value) | Parameters | Successful rates | Percentage |
|---|---|---|---|
| WT | ED=1.15, CTD-Core=74, TMD-TMD=0.2 | 7/8 | 100.0% |
| Smaller ED | ED=1.1, CTD-core=75, TMD-TMD=0.2 | 5/8 | 71.4% |
| No TMD-TMD | ED=1.15, CTD-Core=80 | 6/8 | 85.7% |
| No TMD-TMD + Smaller ED | ED=1.1, CTD-Core=80 | 4/8 | 57.1% |

316 In these simulations, we varied the CTD-Core interaction and selected the value that yielded the highest
317 success rate.
318
319 **Budding of an Imperfect Icosahedral Core Through the Membrane**
320 Recent experimental studies have indicated that the capsid structure of CHIKV during budding
321 does not exhibit perfect icosahedral symmetry[2]. To investigate this effect, we constructed a core
322 with one missing pentamer, introducing an imperfect geometry. As it will be explained later, we
323 tested this core under both wild-type conditions and in simulations corresponding to mutations that
324 abrogate CTD-core and spike-spike interactions.
325 Compared to the core with perfect symmetry, the imperfect core yielded lower success
326 rates. Nevertheless, under optimal conditions, using ED = 1.15, a CTD–Core interaction strength
327 of 77 $k_BT$, and a TMD-TMD = 0.1 $k_BT$, we observed that spikes near the region of the missing
328 pentamer were still correctly positioned, as shown in Figure 6, which illustrates the budding of an
329 imperfect core through the plasma membrane. Reductions in ED size and weakening of the TMD-
330 TMD interactions disrupted T = 4 symmetry by impairing inter-trimer contacts. However, the
331 overall efficiency of assembly was consistently lower. In the WT system with an imperfect core,
332 only 2 out of 12 simulations produced a successful configuration—about 17%—and the success
333 rate declined further when both the ED size was reduced and the TMD-TMD interactions were
334 removed.
335

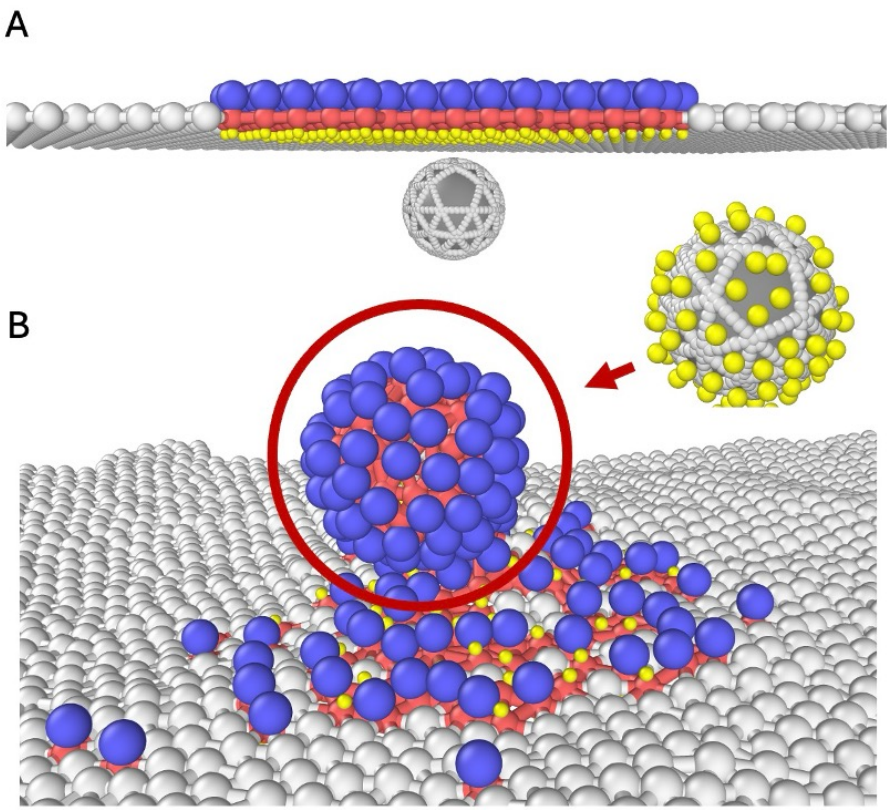


**Figure 6.** *Configurations of the membrane and an imperfect core with icosahedral symmetry.* **A)** The initial state of the system with an imperfect core. **B)** Final state of the system after budding. The inset shows CTD particles and the core. The system parameters include a CTD–core interaction strength of 77 $k_BT$ and a TMD-TMD interaction strength of 0.1 $k_BT$. The particle diameters are set to 1.15 for ED, 0.8 for TMD, and 0.4 for CTD.

The relatively low success rate observed in our simulations, compared to experimental results[2], likely stems from the limitations of the current model, which has a fixed core size and immobile subunits. Experimental data suggest that the initial core is smaller than the final assembled structure, indicating that core subunits can locally dissociate and reassociate to achieve near-perfect icosahedral symmetry. In this study, our aim was not to model this type of computationally costly rearrangement, but rather to test whether spike proteins can still assemble

349 into an icosahedral shell in the presence of core defects, and to evaluate the roles of spike–spike
350 and spike–core interactions in this process.

351 Capturing the dynamic remodeling of the core—from an imperfect to an icosahedral
352 symmetric structure—requires a model that explicitly allows internal rearrangement of capsid
353 subunits [45]. Simulating this process is computationally intensive, as it involves dissociation and
354 reassociation events that must overcome significant free energy barriers [46]. However, such local
355 restructuring is essential for correcting geometric imperfections during budding and achieving
356 stable icosahedral symmetry. In future work, we plan to develop models that incorporate core
357 flexibility and explicitly examine the role of the genome[47] in promoting protein rearrangement and
358 structural maturation.

359 While the theoretical model and simulations provide mechanistic insight into how specific
360 interactions contribute to CHIKV assembly, they necessarily simplify certain aspects of the
361 biological system, such as membrane heterogeneity and the dynamic behavior of viral proteins. To
362 assess the biological relevance of our findings and examine how these interactions function in a
363 cellular context, we next designed targeted mutational experiments to test the roles of
364 glycoprotein–glycoprotein and glycoprotein-core interactions in budding and infectivity.

365

366 **The infectivity of CHIKV depends on multiple interactions between glycoproteins.**

367 To complement and validate the predictions of the coarse-grained simulations, we constructed
368 three CHIKV mutants. To disrupt the intertrimer interactions, we removed a glycosylation site in
369 E2 via the mutation N263Q (intertrimer surface mutant or ITS), and to weaken spike–core
370 interactions, we introduced a double mutation in E2: Y400K/L402R (cytoplasmic tail mutant or
371 CT). To disrupt the intradimer (E1/E2) surface, we added a glycosylation site in E1 through the

372 mutation K245N/R247T (intradimer surface mutant or IDS). The ITS and CT (Y400K/L402R)
373 mutants correspond to interaction changes examined in our coarse-grained simulations. The effect
374 of the IDS mutation was not studied in the simulations but was included experimentally to further
375 test the role of spike–core coupling.

376 Figure 7 shows a Cryo-EM reconstruction (PDB 3j2w) of the asymmetric subunit of
377 CHIKV, depicting the positions of amino acids targeted for mutation to remove or add
378 glycosylation sites, and to convert two hydrophobic residues to hydrophilic ones. To investigate
379 the role of the E1-E2 heterodimer interface, we first generated an E1 double mutant K245N/R247T
380 (CHIKV IDS) (Figure 7A). This mutation creates a glycosylation site at the interface between E1
381 and E2, where the added carbohydrate is expected to introduce steric hindrance that weakens
382 and/or destabilizes the E1/E2 heterodimer. For other Alphaviruses, it has been shown that replacing
383 the hydrophobic amino acids in E2 that interact with the core with basic residues can inhibit
384 budding[26, 48]. To this end, we generated the E2 double mutant Y400K/L402R to block the
385 interaction between the core and the glycoproteins (Figure 7B) (CHIKV CT). Finally, we mutated
386 N263 to a Q in E2 (CHIKV ITS) to remove the glycosylation site at the outer part of the trimer of
387 heterodimers (Figure 7C). The goal was to decrease the interaction between trimers by removing
388 the carbohydrates in this interface; we hypothesize that these carbohydrates stabilize the trimers
389 by steric repulsions. Figure 7D is a schematic representation of the three interactions studied here,
390 and Figure 7E depicts some of the most likely effects of the mutations E1 K245N/R247T, E2
391 Y400K/L402R, and E2 N263Q on these interactions.
392

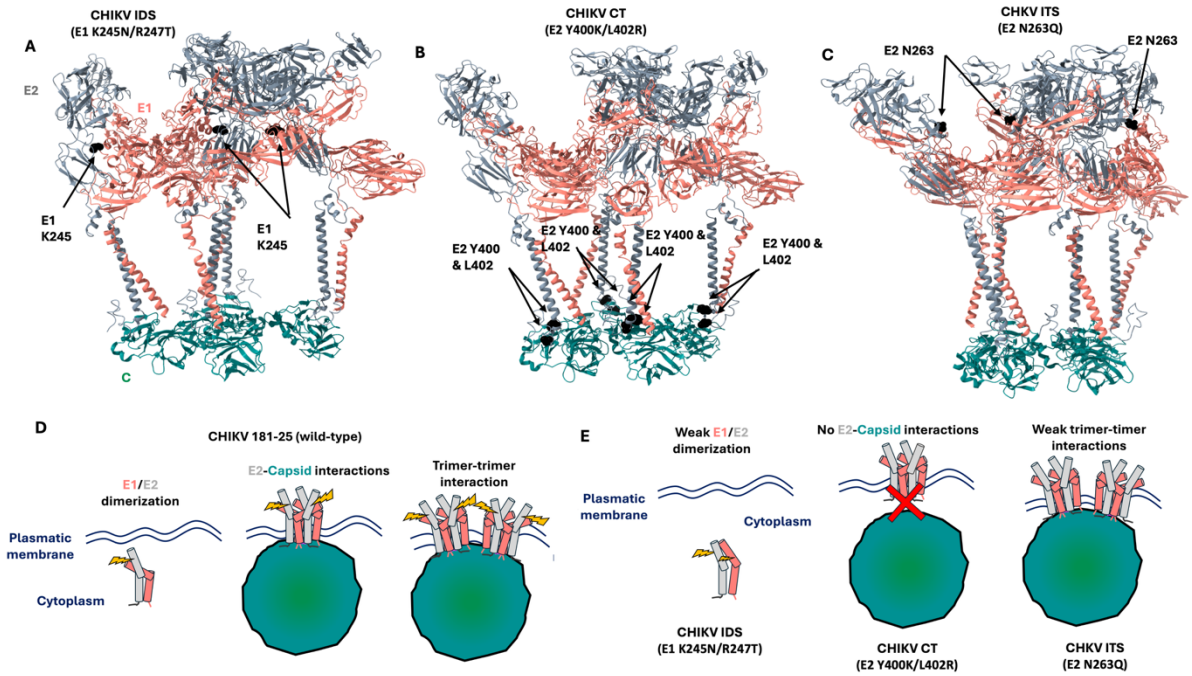


**Figure 7.** *Structure of Chikungunya virus* A-C) Cryo-EM (PDB 3j2w) structure of the T = 4 icosahedral asymmetric unit of CHIKV virion with E1, E2, and C in salmon, gray, and teal. A) E1 K245 is at the interface between E1 and E2. B) The association of E2 with C is driven mainly by a hydrophobic pocket of E2 and Capsid (C). C) E2 N263 is glycosylated and might result in steric interactions between two E2 proteins at the trimer-trimer interface. D-E) Schematic representation of the interaction between glycoproteins and the core during assembly and budding. D) E1 and E2 dimerize in the cytoplasm, and once the glycoproteins are at the plasma membrane, they interact with the CHIKV cytoplasmic core, then the neighboring trimers interact with each other through high-molecular weight sugars at the E2 N263 site, E) In CHIKV IDS, a new glycosylation site was introduced in E1 amino acid 245; this mutation aims to decrease the E1/E2 heterodimer formation. CHIKV CT was designed to inhibit the interaction between E2 and the core by removing the hydrophobic pocket in E1 Y400/Y402. In CHIKV ITS, the N263 glycosylation site was removed to weaken the trimer-trimer interactions.

**Determining the relative infectivity of mutants compared to WT using a reporter virus system.**

To determine the effect of each mutation on virion assembly and budding, we first transfected HEK-293T cells with CMV-driven CHIKV plasmids, based on the attenuated strain CHIKV 181/25 (from here and on referred as WT). These plasmids contain a reporter gene (mKate2), between the C and E3 genes, that is post-translationally cleaved and thus is produced in a 1:1:1:1:1 ratio with respect to C:mKate2:E3:E2:E1. Therefore, the amount of reporter gene is proportional to the number of structural proteins being translated in either a transfected or infected cell. Then, HEK-293T cells were infected with the virus produced by transfection. At 24 hours post-infection (h.p.i.), the amount of virus produced by the transfection was determined by fluorescence microscopy as a relative infectivity to the WT. Each infection was done in triplicate and with four biological replicas.

Figure 8A-D shows representative fluorescence images of infected cells (mKate2-positive). Figure 8A shows that at 24 h.p.i. most cells are mKate2-positive cells (WT infected), while panels B, C, and D show that the number of infected cells with CHIKV IDS, CT, and ITS is extremely low compared to the WT.

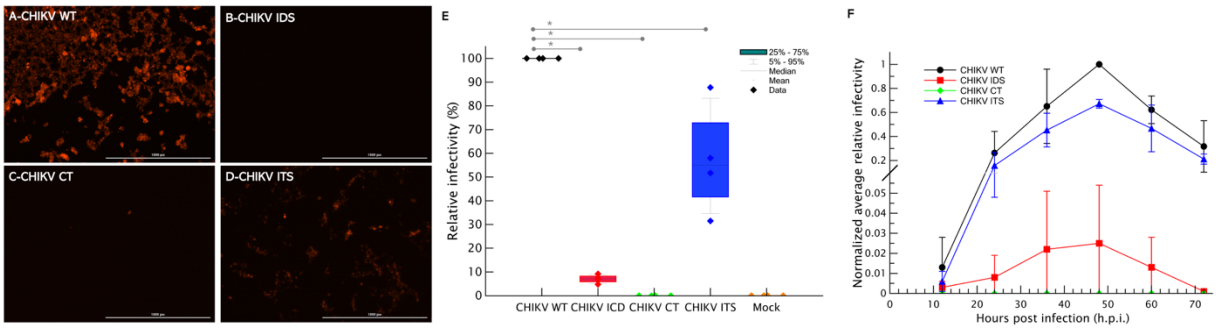


**Figure 8.** *The infectivity of the viral particle depends on several protein-protein interactions.* Representative fluorescent micrographs of HEK-283T cells infected with WT, IDS, CT, and ITS CHIKV viruses. The genome of all these viruses has mKate2 as a reporter gene between the capsid and E3. A-D) Cells infected with the WT, IDS, CT, and ITS viruses, respectively. E) Relative infectivity of each mutant

429 with respect to the WT virus. The relative infectivity was determined by measuring the fluorescence and
430 area of the mKate2-expressing cells using a LionHeart FX automated microscope: 25 images per well, three
431 wells per sample, and four biological replicas. The medians represent values from four experiments (n=4).
432 K-W analysis with Dunn's post hoc showed differences in infectivity for the three mutants compared to the
433 WT. The mutants showed a decrease in the relative infectivity of approximately 50%, 90%, and 100%,
434 respectively, for ISD, CT, and ITS (* $p<0.05$). F) Viral infection kinetics. The infection of WT, IDS, and
435 ITS reaches a maximum at 48 hours post-infection, suggesting that the differences in infectivity due to
436 differences in Gibbs free energy are not due to a kinetic effect. This graph was made by averaging three
437 independent experiments; the graph for each independent experiment is in the supplementary information,
438 and the data were normalized with respect to the average relative infectivity of CHIKV CT at 48 h.p.i. The
439 bars indicate the standard deviation.
440
441 The relative infectivity of these mutant CHIKV viruses compared to the WT is shown in
442 Figure 8E. In contrast, CHKV IDS (E1 K245N/R247T) and CHIKV CT (E2 Y400K/L402R) are
443 about 90% and 100% less infectious than the WT, respectively, while CHIVK ITS (N263Q) is
444 about 50% less infectious than the WT. These results show that blocking the interaction between
445 the core and E2 (CT) decreases the relative infectivity below the detection limit. It has been
446 proposed that E2-core interaction is necessary for assembly [48]. However, the data in Figure 8E
447 suggest that this interaction is insufficient; altering, at least, the interactions between monomeric
448 E1 and E2 and between trimers also decreases the infectivity. These data suggest that these
449 interactions are also required to generate infectious particles.
450 These data suggest that the CHIKV mutants exhibit lower infectivity than the wild type
451 (WT), likely due to defects in assembly and/or particle release. However, it is also possible that
452 these mutations affect genome replication, which in turn could impact assembly efficiency. To

453 address this, infections with CHIKV WT, IDS, CT, and ITS were monitored over a 72-hour period,
454 with measurements taken every 12 hours. Figure 8F shows the normalized average area of infected
455 (mKate2-positive) cells from three independent experiments. These results indicate that the peak
456 of normalized relative infectivity occurs at 48 hours post-infection (h.p.i.) for CHIKV WT, IDS,
457 and ITS. In contrast, CHIKV IDS and CT mutants show minimal, if any, replication, and this
458 deficiency is not rescued even by 72 h.p.i. Notably, if genome replication were significantly
459 impaired by these mutations, we would expect the infectivity peak to be delayed to later time points
460 post-infection. Therefore, it is reasonable to conclude that the differences in infectivity between
461 the CHIKV WT, ITS, and IDS are not due to differences in the kinetics of replication but are related
462 to assembly/budding defects.
463
464 **Budding of CHIKV particles depends on multiple interactions.**
465 To determine which stage of the infectious cycle is affected by the mutations E1 K245N/R247T,
466 E2 Y400K/L402R, and E2 N263Q, we analyzed transfected cells using thin-section transmission
467 electron microscopy (TEM) (Supplementary Figure 3), focusing specifically on how these
468 mutations impact virion assembly and budding. CHIKV IDS and CT mutants exhibit 90% and
469 100% reductions in infectivity relative to WT, respectively, making it extremely challenging to
470 identify infected cells. Moreover, if these mutations severely impair assembly and result in very
471 low infectivity, it becomes nearly impossible to confirm infection status in individual cells based
472 solely on thin-section TEM. Nonetheless, cells infected with alphaviruses can often be identified
473 by the presence of cytopathic vesicle type I (CPV-I), a characteristic marker observable by TEM[7].
474 Supplementary Figures 4A-D show the presence of CPV-I (arrows) in cells infected with the four

475 types of viruses. Once these vesicles were found, we searched the area around the plasmatic
476 membrane of that cell to characterize any possible assembly and or budding process.
477
478 Figure 9 shows characteristic budding events that result in the doubled-layer icosahedral
479 viral particles. Figure 9A shows a CHIKV WT virion budding (red arrow) and an extracellular
480 virion. CHIKV IDS has a relative infectivity of 90% lower than the WT, and, unlike WT or ITS,
481 most budding particles are "stuck" in the initial budding stages (Figure 9B); interestingly, most
482 CHIKV IDS particles are stuck in the initial stages of budding, forming a group or collection of
483 incomplete budding structures close to each other. These incomplete budding structures are very
484 similar to the snapshot of the MD simulation in Figure 4B. The fact that we found some partial
485 virions suggests that the E1 K245N/R247T mutation did not completely block the E1/E2
486 heterodimer formation, which is also consistent with our MD results. As expected, we could not
487 find any budding particles for CHIKV IDS. Figure 9C shows that the cores remain cytoplasmic;
488 in fact, it is much more likely to observe cytoplasmic cores in cells transfected with CHIKV CT
489 than with any other mutant. Figure 9D shows one extracellular CHIKV ITS particle and two still
490 bound to the plasmatic membrane.
491
492

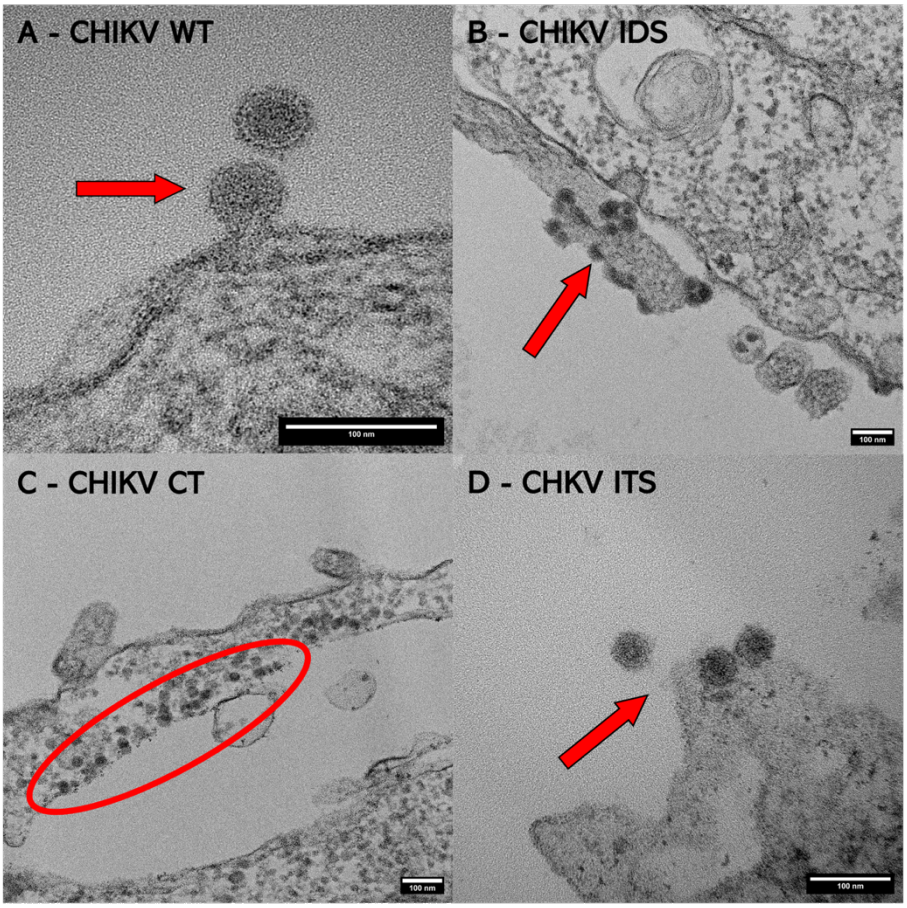


**Figure 9.** *Budding structures of WT and mutant viral particles.* Thin-section transmission electron micrographs of HEK-293T cells infected with the WT, IDS, CT, and ITS, CHIKV viruses showing budding events of the virions (A, B, and D). The WT, IDS, and ITS viruses bud by forming a neck, which will eventually be pinched off, releasing the virus to the extracellular medium (arrows). C) CHIKV CT does not bud out, and all the cores remain in the cytoplasm (red oval).

**Virion morphology depends on the strength of the interactions between the glycoproteins.** To determine if weakening the interaction between trimers, by removing the "molecular handshake" between them (CHIKV ITS), alters the particle morphology, we measured the hydrodynamic diameter of purified CHIKV WT and ITS particles purified from serum-free Vero E6-infected cells. The purified samples were resuspended in PBS, and their hydrodynamic

505 diameter was determined by dynamic light scattering (DLS). This analysis was performed using
506 two biological replicates and three experiments per replicate. Figures 10A and B show the
507 hydrodynamic diameter distribution for two independent purifications (batches) of CHIKV WT
508 and ITS, respectively. The broken and solid lines indicate the measurements for batches 1 and 2,
509 respectively. The average hydrodynamic diameters for the WT and ITS CHIKV virions are 67 nm
510 +/- 3 nm and 113 +/- 10 nm, respectively. Furthermore, these experiments show that purified
511 CHIKV ITS virions are heterogeneous compared to CHIKV WT virions. These data are consistent
512 with the trends observed in Figures 4 and 10 and support the hypothesis that removing this
513 glycosylation site makes the viral particle less stable and homogenous, decreasing trimer-trimer
514 interactions. Figures 10C and D show positive-stain TEM images of purified CHIKV WT and ITS
515 from batch 1, respectively.
516

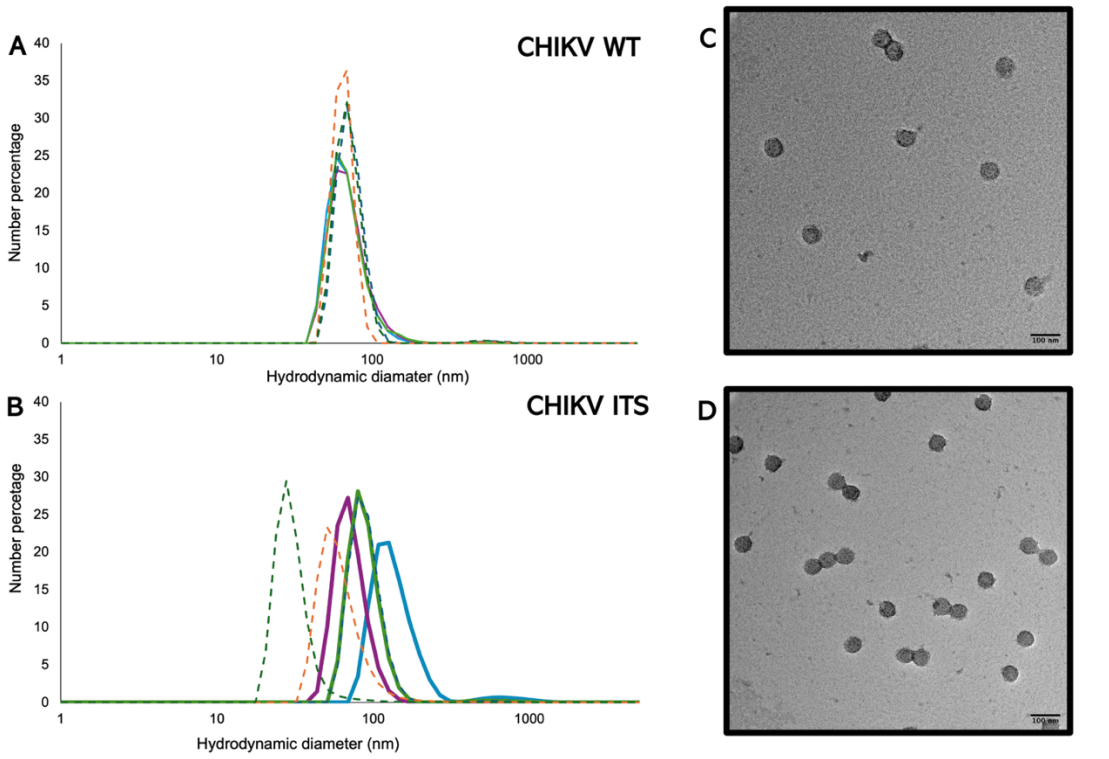


517

518 **Figure 10.** *Removing the E2 N623 glycosylation site increases particle heterogeneity.* Vero E6 cells were
519 infected with either WT or ITS virus in fetal bovine serum-free media; they were purified by low-speed
520 centrifugation, resuspended in PBS, and the hydrodynamic diameter (nm) was determined by using
521 dynamic light scattering (DLS). A) Three measurements of the hydrodynamic diameters of the WT virus
522 from two independent batches (broken lines are batch 1 and solid lines are batch 2). B) Three measurements
523 of the hydrodynamic diameters of ITS from two independent batches, broken lines are batch 1, and solid
524 lines are batch 2. For the WT distribution, one hydrodynamic radius is extremely homogenous (67 nm +/-
525 3 nm), while the ITS is highly heterogeneous (113 +/- 10 nm). These data suggest that virions with weak
526 trimer-timer interactions are no longer homogeneous. C-D) Negative-staining TEM images from the
527 purified samples used for the DLS measurements for batch 1.

528 The data shown here suggest that altering the interaction between glycoproteins decreases
529 the ability of the particles to bud from the producer cells. Therefore, we analyzed the cellular
530 localization of 500 virions/cores for CHIKV WT, IDS, and ITS of transfected cells by thin-section
531 EM. These localizations were defined as cytoplasmic, budding, and extracellular particles; the
532 cytoplasmic particles are cores that are not interacting with the plasmatic membrane, the budding
533 particles are those forming any type of neck or protrusion, and the extracellular particles are the
534 released virions. The distribution of virions in Figure 11 shows that most CHIKV WT particles are
535 either at the budding stage or released (extracellular). Very few particles remain as cytoplasmic
536 cores.

537

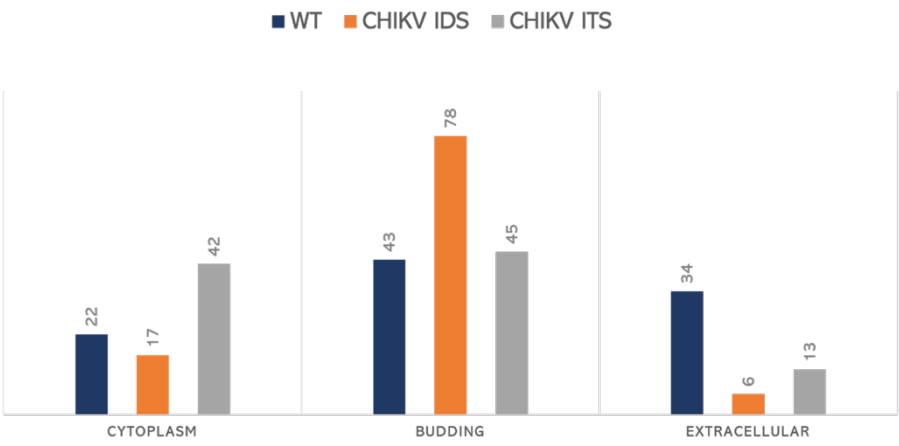


**Figure 11.** *Relative distribution (percentage) of virions in different cellular compartments*. CHIKV WT (blue bar) is predominantly found in both budding at the plasma membrane and in the extracellular space. In CHIKV IDS (orange bar), which has about 2-fold fewer infections than the WT, the distribution of virions is similar to the WT. However, for CHIKV ITS (grey bar), most virions were found budding, while the amount of cytoplasmic and extracellular material was the lowest of these three viruses. These data suggest that weakening E1-E2 interactions results in defects in the budding, most likely by increasing the energy required for the core and glycoproteins to deform the plasma membrane and bud out.

Figure 11 shows that when the E1/E2 heterodimer interface is altered by adding a glycosylation site, most particles are found at the plasma membrane at some stage of budding. This suggests that the mutant's inability to form proper trimers of heterodimers (later interactions) almost completely blocks the particle from pinching off the plasma membrane. As expected, from the WT, IDS, and ITS particles, the WT are the most abundant in the extracellular space, with only about 1/3 of the CHIKVK ITS with respect to the WT are found outside the cell, which is consistent with the relative infectivity data and the MD simulations (*i.e.,* Table 1).

Based on the results of our simulations and from the DLS data and virion localization in the cell, we hypothesize that the carbohydrates at the interface of two trimers generate steric

557 repulsion between trimers that contributes to the icosahedral ordering of the trimers. This steric
558 interaction was first proposed for another Old-World Alphavirus, Mayaro virus, and described as
559 a "molecular handshake" between glycans of two different trimers [31]. Therefore, removing the E2
560 glycosylation site at N263 is expected to decrease the stability of the viral particles. To test this,
561 we analyzed the stability of the particles to heating by taking the supernatant from transfected
562 cells, dividing into aliquots, and incubating them at 37 °C, 40 °C, 45 °C, 50 °C, 55 °C, and 60 °C
563 for 30 minutes. The samples were then cooled to 37 °C for 5 minutes and used to infect HEK-293T
564 cells. The relative infectivity was determined by normalizing the areas of fluorescent cells
565 (mkate2-positive cells) for each virus type with the sample incubated at 37 °C for that virus type
566 (Figure 12). The relative infectivity of WT CHIKV WT at 40ºC and 45ºC, compared to the CHIKV
567 WT sample incubated at 37ºC, remained constant, but there was a significant drop in relative
568 infectivity around 50ºC. Interestingly, CHIKV ITS is far more sensitive to changes in temperature
569 compared to a sample of CHIKV ITS incubated at 37ºC. As soon as the samples were heated, the
570 relative infectivity decreased. This data was fitted with an equation that assumes a cooperative
571 dissociation process. This model has two parameters: the temperature at which the relative
572 infectivity decreases by 50% ($T_{RI50}$) and a cooperative exponent (n). The values of $T_{RI50}$ and n for
573 CHIKV WT and ITS were 50ºC and 99, and 44ºC and 16.5, respectively. These parameters suggest
574 that removing the glycan in E2 N263 significantly affects the particle stability. Experiments using
575 twice the amount of CHIKV ITS compared with WT yielded the same results (data not shown).
576 Furthermore, the decrease of the cooperative exponent (n) suggests that the dissociation process
577 of the virion of the CHIKV ITS is less ordered and might involve a weaker interaction than CHIKV
578 WT.
579

580

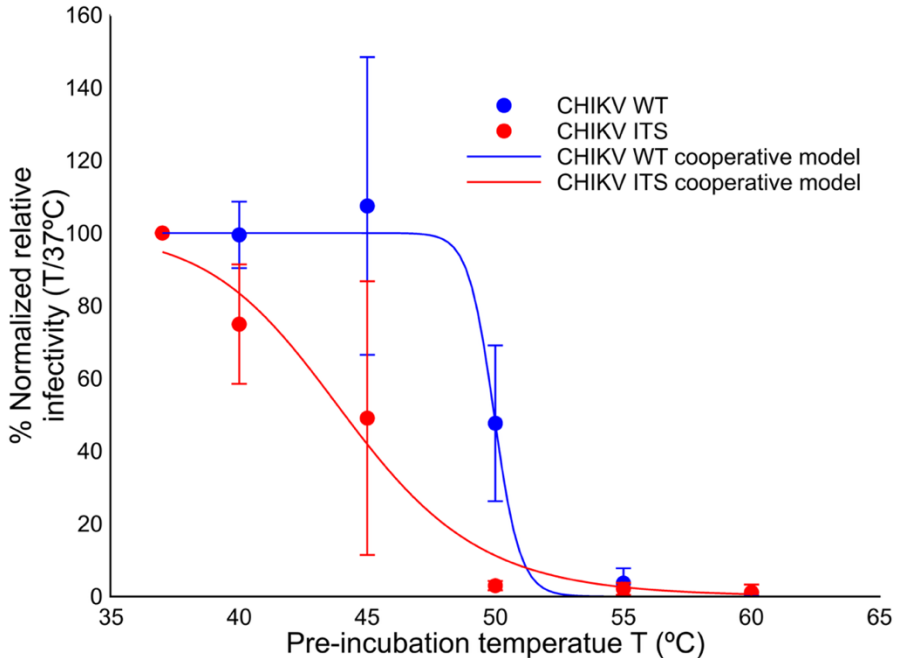


581

582 **Figure 12.** *The thermal stability of the virions depends on trimer-trimer interactions.* The relativity of the
583 WT and ITS viruses was calculated with respect to the area and fluorescence of infected cells for each virus
584 at 37ºC. The circles and bars are the mean and standard deviation of three independent experiments. On the
585 one hand, the relative infectivity of WT remains constant from 37ºC to 45ºC, reaching a 50% decrease at
586 50ºC. On the other hand, when the trimer-trimer interactions are weakened (CHIKV ITS) the infectivity
587 starts to decrease at 40ºC, reaching a 50% decrease at 45ºC. These data suggest that weakening trimer-
588 trimer interactions decreases the thermal stability of the viral particle. The data was fitted with a cooperative
589 model that follows Hill's equation for competitive binding $RI = 100/(1+(T/T_{RI50})^n)$ where RI, T, $T_{RI50}$, and
590 n are the relative infectivity normalized with the relative infectivity at 37ºC, Temperature at which the virus
591 was incubated, the Temperature at which the relative infectivity decreases by 50%, and a cooperative
592 coefficient. For the WT, the $T_{RI50}$ and n are 50ºC and 99, respectively, while for the ITS mutant, they are
593 44ºC and 16.5.

594

595 **DISCUSSION**

596 In this paper, we set out to determine how specific protein–protein interactions govern the
597 assembly and budding of Chikungunya virus (CHIKV). We hypothesized that the assembly and
598 budding of CHIKV viral particles depend not only on the canonical E2-core interactions [3, 26, 35] but
599 also on other protein-protein interactions. Thus, our goal was to dissect the roles of E2–core
600 coupling, E1–E2 heterodimerization, and trimer–trimer (spike-spike) interactions in shaping the
601 formation of stable and infectious virions. To achieve this, we combined coarse-grained
602 simulations with site-directed mutagenesis of a CHIKV system with a reporter gene analysis
603 targeting key interfaces within the CHIKV glycoprotein layer.

604 Our simulations revealed that efficient budding requires a finely tuned balance between
605 spike–core attraction and lateral glycoprotein interactions. Although this is not the first model to
606 try describing Alphavirus budding, it addresses novel interactions between the ectopic domains of
607 trimers that have not been previously explored and compared with experimental data[30].

608 First, interactions between the CTD domain of the spikes and the underlying nucleocapsid
609 core were essential for initiating membrane deformation. When the strength of this interaction was
610 reduced below a critical threshold, budding was arrested—consistent with experimental results for
611 CHIKV CT (E2 Y400K/Y402R), which disrupts the hydrophobic pocket in E2 that binds to a
612 hydrophobic pocket on the nucleocapsid core—leading to complete loss of budding and virion
613 assembly. The effect of this mutation has been demonstrated elsewhere[3, 26, 35] and prompted the
614 proposal that E2-core interactions primarily drive Alphavirus budding. However, the simulations
615 and experiments presented here show that this interaction is necessary but not sufficient for
616 assembly and budding.

617 Beyond initiating budding, interactions among glycoprotein trimers were found to be
618 critical for achieving proper spatial organization. Simulations showed that spike–spike interactions

619 alone could not guide self-assembly toward the correct geometry, nor could a smooth spherical
620 core. However, an icosahedral core with T = 4 symmetry was sufficient to support the correct
621 positioning of glycoproteins, even when imperfect (*e.g.,* missing a pentamer). Notably, the absence
622 of ED-ED interactions significantly reduced budding efficiency, mirroring experimental results for
623 CHIKV ITS (E2 N263Q), in which deletion of a glycosylation site weakens trimer–trimer
624 interactions and leads to virions with diminished infectivity, an increase in particle heterogeneity,
625 and a decrease in particle stability. Despite a previous suggestion that spike-spike proteins between
626 ecto domains through glycans in E2 N263 confer stability to the particle[31], the effect of this
627 interaction has not been previously explored either through simulation or experiments.

628 Although our model does not resolve detailed E1–E2 heterodimerization, experimental
629 analysis of CHIKV IDS (E1 K235N/R247N), which introduces a glycosylation site in E1 at the
630 heterodimer interface, revealed profound assembly defects. These particles were largely non-
631 infectious, rarely completed budding, and accumulated at the plasma membrane, suggesting that
632 stable heterodimer formation is essential for trimer assembly and for progression beyond the early
633 stages of particle envelopment and release from the plasma membrane.

634 To explore the role of core structure, we also simulated budding from a defective core
635 lacking one pentamer. While budding was still possible under favorable conditions, the success
636 rate declined compared to simulations with a fully symmetric core. These findings are consistent
637 with cryo-ET data, which show that one pole of the CHIKV virion can initiate budding despite
638 exhibiting structural defects[18]. This observation highlights the importance of geometric
639 compatibility between the core and the glycoprotein shell. It is important to note that our current
640 model assumes a fixed-size, rigid core and does not allow subunit rearrangement during assembly.

641 However, cryo-ET data[2] suggest that the CHIKV core may undergo remodeling during budding,
642 transitioning from an irregular structure in the cytoplasm to a more symmetric state at the plasma
643 membrane. Incorporating such dynamic remodeling in future simulations will provide a more
644 complete picture of CHIKV morphogenesis. Furthermore, our group is performing site-directed
645 mutagenesis experiments of the CHIKV core to understand how defective nucleocapsids affect
646 budding and particle release.

647 Although high-resolution cryo-EM maps for CHIKV [2, 37, 49-52] do not show electron density
648 corresponding to high-molecular-weight glycans at E2 N263, our experimental results support a
649 structural role for this glycosylation site, in agreement with the "*molecular handshake*" model
650 proposed for Mayaro virus[31] . Deletion of this glycan in CHIKV (E2 N263Q) impairs trimer–trimer
651 interactions and reduces the cooperativity of disassembly upon heating. The apparent discrepancy
652 between structure and function may stem from the higher particle heterogeneity observed in
653 CHIKV[18, 37] , which could obscure this glycan in ensemble-averaged cryo-EM reconstructions.

654 While previous simulations and experiments have shown that glycoprotein spikes alone
655 cannot reliably assemble into icosahedral structures[30], some experimental studies suggest that
656 capsid proteins can form T=4 icosahedral shells prior to budding[15, 17]. However, due to technical
657 limitations, these studies have not been able to definitively confirm the symmetry of the pre-
658 budding core. More recent experiments indicate that when the core deviates from perfect
659 symmetry[18], interactions between capsid proteins and spikes—as well as lateral spike–spike
660 contacts—can help stabilize or guide the assembly toward icosahedral order. Our simulations
661 revealed that non-icosahedral core geometries are mechanically constrained; these structures often
662 fail to progress, then disassemble and reassemble into more symmetric configurations. These
663 findings suggest that local rearrangement of the core may be required for the formation of stable

icosahedral particles, which is consistent with the cryo-ET data from Chmielewski et al[2]. Although the current model used in this study employs a fixed, preassembled core, we speculate—based on previous simulations and supporting experimental observations—that in *vivo*, capsid subunits may locally dissociate and reassociate during budding to correct geometric imperfections and promote icosahedral symmetry. Future simulations incorporating core flexibility and experiments mutating the amino acids of the cytoplasmic core will be essential to fully capture this dynamic aspect of alphavirus assembly.

## CONCLUSIONS

Our integrated computational and experimental study demonstrates that CHIKV assembly and budding are governed by a coordinated network of protein–protein interactions operating across multiple spatial and temporal scales. More significantly, this work highlights the power of simulation-guided mutagenesis as a rational strategy to dissect and reprogram virus assembly. By selectively altering key interaction interfaces, we gain deep molecular insights without the need for atomistic simulations or exhaustive mutational screens.

Disrupting E2–core attraction, E1–E2 heterodimerization, or trimer–trimer contacts impairs assembly through distinct but complementary mechanisms—preventing budding, disrupting trimer formation, or destabilizing the glycoprotein lattice. These results counter the view that E2–core interactions alone are sufficient for particle formation; instead, they are necessary but not sufficient. Our simulations emphasize the essential roles of both vertical (core–glycoprotein) and lateral (inter-spike) interactions, including E1–E2 contacts and steric repulsions between adjacent trimers, in enabling budding and the emergence of T = 4 icosahedral symmetry.

While this study focused on perturbing E1–E2 and intertrimer interfaces, additional interactions—such as E1–E1′ and E2–E2′ contacts—are also likely to contribute to lattice stability and proper assembly. Introducing a glycosylation site into E1, as in CHIKV IDS, significantly reduced infectivity, further underscoring the delicate balance of interactions required for efficient particle formation.

A more comprehensive understanding of glycoprotein interactions will be essential for building a complete and predictive model of alphavirus assembly—one that incorporates mechanistic diversity across viral lineages and explains variations in budding efficiency and infectivity between Old- and New-World alphaviruses. Taken together, our findings support a unified model in which vertical and lateral interactions act in concert to shape virion formation, offering a strategic foundation for therapeutic interventions that target the assembly and release of infectious virus particles.

# METHODS AND MATERIALS

## Coarse-grained simulations

To simulate CHIKV budding through the plasma membrane, we developed a model incorporating a fluid membrane, spike proteins, and the viral core, as described below.

***Fluid membrane:*** We model the biomembrane as a triangular lattice[53], as illustrated in Supplementary Figure 1. The energy of this network includes contributions from both bond stretching and bending[54]. The stretching energy is represented by a harmonic potential summed over all bonds:

$$E_s = \sum_{bonds} \frac{1}{2} k_s (r - a)^2, \quad \textbf{Eq. 1}$$

here, $a = 10\ nm$ is the equilibrium length of the spring. The parameter $k_s = 25\ k_B T * nm^{-2}$ is the stretching modulus. The bending energy is calculated by summing over all pairs of triangular subunits that share an edge, and is given by:

$$E_b = \sum_{pairs} k_b\,(1 - \cos(\theta - \theta_0)),\ \textbf{Eq. 2}$$

where $\theta_0 = \pi$ is the preferred dihedral angle, and $k_b = 20\ k_B T$ is the bending modulus.

To ensure the incompressibility of our coarse-grained membrane, we have placed a spherical LJ potential particle, denoted by M (see Supplementary Figure 1), with a diameter $a$ at each membrane vertex. Membrane fluidity is achieved by performing Monte Carlo (MC) simulations with the bond-flipping method, which permits dynamic changes in the membrane's connectivity[55, 56]. The procedure for bond flips is illustrated in Supplementary Figure 2. Each MC step consists of $N_b$=8781 attempts, where $N_b$ is the total number of bonds. In each attempt, a randomly selected bond connecting two adjacent triangles is removed and reattached between two previously unconnected vertices, as shown in Supplementary Figure 2. These moves are designed to preserve the total number of vertices and bonds, thereby maintaining the overall topology of the membrane. By allowing lateral rearrangements of connectivity, they facilitate the diffusion of topological defects across the membrane.

***Spike proteins:*** Each coarse-grained spike represents a trimer of heterodimers, as illustrated in Figure 1. It comprises three components: ED (ecto domain, blue), TMD (transmembrane domain, red), and CTD (C-terminal or cytosolic domain, yellow). ED protrudes outward from the membrane into the lumenal/extracellular-facing side of the budding virus; TMD is hydrophobic

729 and embedded within the lipid bilayer; and CTD is located on the cytosolic side, where it interacts
730 with the viral core.
731
732 ***Core Particles:*** The capsid of CHIKV is illustrated in Figure 2. In our model, we use three types
733 of core particles. In all three types of cores, the sphere part has a diameter of 3.2a (see Eq. 1). The
734 first is a simple spherical core (Figure 2A) that interacts with the C-terminal domain of the spike
735 proteins (the yellow domain in Figure 1). The second core (Figure 2B) is also spherical and
736 interacts specifically with the CTD of the spike proteins. Its surface exhibits icosahedral symmetry
737 and consists of 80 triangular faces. Note that only the spherical surface directly interacts with the
738 spike proteins, while the triangles interact with them exclusively via steric repulsion. This type of
739 interaction promotes the assembly of spikes into a T=4 shell around the core—an organization that
740 would not occur otherwise. Without such interactions, the proteins would form a shell around a
741 spherical core lacking any particular symmetry, which would be inconsistent with the experimental
742 data. The third core (Figure 2C) is similar in shape and size but lacks icosahedral symmetry due
743 to the absence of a pentamer.

744 ***Interactions***: The attractive interactions between CTD-CTD and the core, as well as between TMD
745 proteins, are modeled using the Lennard-Jones potential,

746 $$E_{lj} = \sum_{<i,j>} 4\epsilon_{ij}\left(\left(\frac{\sigma}{r_{ij}}\right)^{12} - \left(\frac{\sigma}{r_{ij}}\right)^{6}\right) \quad \textbf{Eq. 3}$$

747 where $\sigma = 2^{-1/6}d$ with $d$ the distance between any two particles in contact including, CTD-core
748 and TMD-TMD. $\epsilon_{ij}$ and $r_{ij}$ denote the interaction strength and the distance between particles $i$
749 and $j$, respectively. The interactions are subject to a cutoff distance $r_{cut_1} = 0.5a + d$. In addition,

750 the excluded volume interaction between all particles is presented with a shifted LJ repulsion
751 potential

752 $$E_{lj}^{rep} = \sum_{<i,j>} 4\epsilon_2((\frac{\sigma}{r_{ij}})^{12} - \left(\frac{\sigma}{r_{ij}}\right)^6) + \epsilon_2 \quad \textbf{Eq. 4}$$

753 with $\epsilon_2 = 1$, $r_{cut_2} = d$ and $\sigma = 2^{-1/6}d$.

754

755 **Generation of cDNA constructs for mutant viruses.**

756 The plasmid pACNR-CHIKV is a complete sequence clone of the genome of the Chikungunya
757 181/25 virus (WT) in a CMV-driven plasmid[41]. It allows for the generation of viral progeny by
758 transfecting HEK-293T cells and serves as a template for all mutations. This plasmid contains the
759 mKate2 reporter gene between CP and E3, which is released from the structural polyprotein. The
760 reporter gene is translated from the same subgenomic RNA as the structural proteins, hence there
761 is a 1:1:1:1:1 ratio of CP:makte2:E3:E2:E1 proteins in the cytoplasm; hence the amount of mKate2
762 is proportional to the amount of structural proteins translated in a transfected and infected cell.
763 This protein allows for the relative infectivity of the mutant viruses to be determined by
764 fluorescence microscopy compared to the WT virus. The mutations made are described below:

765 Intradimer surfaced mutant (IDS) is a double mutant in E1 K245N and R247T, the
766 cytoplasmic tail mutant (CT) consists of two mutations in E2 Y400K/L402R, and in the intertrimer
767 surface mutant (ITS), N263 of the E2 protein was replaced by Q. The mutations were performed
768 by site-directed mutagenesis using the protocol by Liu & Naismith[57]. All PCRs were performed
769 using HS Phusion II (ThermoFisher, Inc.), following the vendor's protocol (see Table 3). The PCR
770 products were digested with DpnI (ThermoFisher, Inc.) and analyzed by agarose/TBE gel
771 electrophoresis. *E. coli* DH5a bacteria (New England Biolabs) were transformed with the DpnI-

772 digested PCR products. The selected colonies were cultured in LB (Luria-Bertani) medium with
773 ampicillin, following standard protocols. The clones were purified with Promega's MiniPrep
774 Wizard kit, and the sequence identity was confirmed by Sanger sequencing at
775 LANBAMA/IPICyT.
776

Table 3. Primer sequences used for site-targeted mutations and sequencing.

| Mutant | Primer Name | Sequence |
|---|---|---|
| **CHIKV ITS** | FP-E2N263Q | GGCAcAaGTGACATGCAGGGTGCCTAAGGCAAGG |
| | RP-E2N263Q | CATGTCACtTgTGCCAGAGGAAACGGAATGTGAAC |
| | FP-SeqE2N263Q | CCAGACACCCCAGATCG |
| **CHIKV IDS** | FP-E1KRtNT | AAAtGAAacAGGGGCGTCGCTGCAGCACA |
| | RP- E1KRtNT | CCCCTgtTTCaTTTAGCCAATACTTGAAGCCAG |
| | FP-SeqE1 | TGCACCGCACACTTG |
| **CHIKV CT** | FP-E2Y400K | ACCGaAgGAACgGACACCAGGAGCTACCGTC |
| | RP- E2Y400K | TGTCcGTTCcTtCGGTGTAATGCATCTGCGTCGT |
| | RP-SeqE2Y400K | GATCACTGTTACGTGTTCG |

Note: Lowercase letters on primers indicate nucleotides that will be changed during the site-targeted mutation.

777

778 **Virus rescue through transfection.**

779 The production of infectious and quantification of viral particles is similar to that done with other
780 viruses with reporter genes [58, 59]. HEK-293T cells (ATTC) were grown in DMEM medium
781 (Corning, Inc.) with glucose (1 g/L) and sodium pyruvate (110mg/L) with 10% fetal bovine serum
782 (Sigma-Aldrich, Inc.) at 37ºC and 5% $CO_2$. The transfections were done following the protocol
783 from Colunga-Saucedo et al.[41]. Briefly, transfections were performed in 12-well plates using
784 Lipofectamine 3000 (Invitrogen, Inc.) according to the vendor's protocol, with the modification

785 that 0.6 µg of plasmid was used to transfect 100,000 seeded cells. We always transfected pACNR-
786 CHIKV (positive control) and a mock transfection with lipofectamine, but without any plasmid in
787 each transfection, on the same plate as the mutants. At 24 hours post-transfection (h.p.t.), the
788 supernatant was removed, the cells were washed with PBS, and at 48 h.p.t., the supernatant was
789 collected, filtered using a 0.22 µm syringe filter, and stored at -80ºC in 0.1 mL aliquots. We
790 performed four independent transfections.
791
792 **Assessing infection via a reporter assay.**
793 The quantification of the viral particles produced by transfection was directly determined as the
794 relative infectivity of the mutants to the WT. This was achieved by infecting HEK293T cells in
795 12- or 24-well culture plates in triplicate with 15 and 30 µL of the supernatant from the transfected
796 cells, respectively. Every culture plate used for relative quantification assays contained a positive
797 control (CHIKV 181/25) and a negative control (supernatant of non-transfected cells), both of
798 which were produced in the same transfection as the mutants of interest. The infectivity assays
799 were performed only with supernatants from the same batch of transfected cells, thawed only once.
800 The relative infectivity was measured by quantifying the total area of cells expressing mKate2 at
801 24 hours post-infection (h.p.i.) using an inverted fluorescence microscope LionHeart FX (Biotek,
802 Inc.). 25 images were taken per well (5 x 5 symmetrical grid automatically generated by the
803 microscope) with a 4x objective, using the Texas red filter (excitation 559 nm+/- 34 nm and
804 emission 630 +/- 69 nm) to visualize the cells expressing the reporter gene. The relative infectivity
805 (R.I.) was determined by measuring the area of the fluorescent cells per well, averaging with the
806 total area of each well, and setting the total average area of the fluorescent cells infected with the

807 WT as 100%. At least four independent experiments (n=4) were performed, each in triplicate for
808 each infection scenario.
809
810 **Sample preparation for thin-section EM.**
811 For thin-section Transmission Electron Microscopy (TEM), HEK293T cells were seeded in a 6-
812 well plate, transfected, and fixed with 2% glutaraldehyde in 0.1M cacodylate pH 7.2 buffer for 2
813 hours at room temperature, following a previously published protocol [60]. Briefly, fixed samples
814 were washed three times with 0.1 M sodium cacodylate pH 7.2, then fixed with 1% osmium
815 tetroxide in 0.1 M sodium cacodylate for 1 hour at room temperature and in the dark. Subsequently,
816 they were washed twice with cacodylate buffer and once with 0.1 M sodium acetate pH 4.5. The
817 cells were stained with 0.5% uranyl acetate for 1 hour at room temperature in the dark. Then, they
818 were washed thrice with 0.1 M sodium acetate and thrice with MilliQ water for 10 minutes. The
819 next day, they were dehydrated with ethanol in increasing concentrations (35%, 50%, 70%, 95%,
820 and 100%) for 10 minutes and three times each. The cells were washed three times with EMbed
821 812 resin and cured at 55ºC for 48 hours. The resin discs were cut (70–80 nm thickness) using a
822 diamond blade on a LEICA EM UC7 ultramicrotome, placed on copper grids, and stained with
823 0.5% uranyl acetate and 0.5% lead citrate. The samples were visualized on a JEM-JEOL-2100
824 transmission electron microscope at 200 kV with a 4k GatanOne 4K View camera. The images
825 were analyzed using ImageJ® (NIH) and Fiji (NIH) software.
826
827 **Viral replication kinetics.**
828 The replication kinetics were performed in three independent experiments, each in triplicate, by
829 infecting HEK293 T cells seeded in 24-well plates (50,000 cells per well) with 15 µL of

830 supernatant. The normalized area of the fluorescent cells was measured every 12 hours for three
831 days, taking 25 images per well, using the Texas red filter and a 20x objective. The average
832 fluorescent area of each experiment was normalized to WT, such that the mean fluorescence cell
833 area of the WT was a relative infection of 100%.
834
835 **Thermal stability assays.**
836 To determine the thermal stability of the viral particles, the media collected from the transfection
837 were diluted (15 mL of virus and 85 mL of OptiMem) and incubated at 37°C, 40°C, 45°C, 50°C,
838 55°C, 60°C, and 90°C for 15 minutes and cooled down to 37°C. HEK-293T cells were infected in
839 48-well plates in triplicate. The R.I. of the WT at a temperature different than 37ºC was normalized
840 to that of the WT at 37ºC, and the infectivity of M3-E2 N263Q was normalized with that of this
841 mutant at 37ºC. The average R.I. was plotted as a function of the incubation temperature. The data
842 was fitted with QtiPlot 5.15.2 using Hill's equation for competitive unbinding R.I. =
843 $100/(1+(T/T_{RI50})^n)$ where R.I., T, $T_{RI50}$, and n are the relative infectivity at any temperature
844 normalized the relative infectivity at 37ºC, the temperature at which the virions were incubated,
845 the temperature at which the infectivity decreases by 50%, and a cooperative coefficient,
846 respectively. Each experiment was done in triplicate with four biological replicates.
847
848 **Virus purification and characterization by Dynamic Light Scattering and Transmission**
849 **Electron Microscopy.**
850 The production of CHIKV WT and ITS (E2 N263Q) virions was performed in Vero E6 cells, using
851 two T75 flasks per virus, for a period of three days. The cells were grown in DMEM 10% FBS
852 and antibiotics until they reached 100% confluency (approximately 8 million cells per flask) before

853 infection. Then, the media was replaced with OptiMem, and the cells were infected with 1 ml of
854 virus for each condition. The medium was replaced after two hours, and the media were collected,
855 filtered with a 0.22 µm syringe filter, and stored at 4ºC every 24 hours for three days. The viral
856 particles were purified with a low-speed centrifugation protocol [61]. The following day, the
857 supernatant was recovered, and the pellet was resuspended with 200 µl of PBS.

858 The hydrodynamic diameter of virions was measured by Dynamic Light Scattering (DLS)
859 using a ZETA SIZE PRO Zetameter (Malvern, Inc). Each measurement was done in triplicate with
860 biological replicas (two independent viral productions and purifications).

861 The purified samples were loaded on 100 mesh copper grids covered with Formvar
862 (TedPella, Inc.) following standard protocols, stained with uranyl acetate, and observed in TEM
863 JEM-JEOL-2100 at 200 kV.

864

865 **Statistical analysis**

866 Data analysis was performed using the Statistica 10® program. The Kolmogorov-Smirnov test
867 was used to determine the normality of the data, and the statistical differences in the infectivity
868 data were analyzed with the Shapiro-Wilk test. To determine the existence of significant
869 differences ($p \leq 0.05$), the non-parametric test for multiple comparisons by Kruskal-Wallis,
870 followed by Dunn's post hoc test, was used.

871

872 **ACKNOWLEDGMENT**

873 M.A.C.I. (CVU: 1232434) acknowledges the support of SECIHTI through the Ph.D. fellowship
874 4044561 M.C-G. thanks SECIHTI for the grant CBF2023-2024-1125 and COPOCYT for the grant
875 2024-03-M07. RZ acknowledges support from NSF DMR-2131963 and MCB/PHY-2413062.

876

877 **ABBREVIATIONS**

878 CHIKV, Chikungunya virus

879 CMV, Cytomegalovirus

880 CP, Capsid protein

881 cryo-EM, Cryo-electron microscopy

882 cryo-ET, Cryo-electron tomography

883 CT, Cytoplasmic tail mutant

884 CTD, C-terminal or cytosolic domain

885 DLS, dynamic light scattering

886 ED, Ectodomain

887 h.p.i., Hours post-infection

888 IDS, Intradimer surfaced mutant

889 ITS, Intertrimer surface mutant

890 LJ, Lennard-Jones

891 MC, Monte Carlo

892 MD, Molecular dynamics

893 NC, Nucleocapsid or core

894 PBS, Phosphate-buffered saline

895 TMD, Transmembrane domain

896 TEM, Transmission Electron Microscopy

897 WT, Wild-type

898

## REFERENCES


1. Ruiz-Herrero, T.; Velasco, E.; Hagan, M. F., Mechanisms of budding of nanoscale particles through lipid bilayers. *J Phys Chem B* **2012,** *116* (32), 9595-603.

2. Chmielewski, D.; Schmid, M. F.; Simmons, G.; Jin, J.; Chiu, W., Chikungunya virus assembly and budding visualized in situ using cryogenic electron tomography. *Nat Microbiol* **2022,** *7* (8), 1270-1279.

3. Byrd, E. A.; Kielian, M., The Alphavirus E2 Membrane-Proximal Domain Impacts Capsid Interaction and Glycoprotein Lattice Formation. *J Virol* **2019,** *93* (4).

4. Byrd, E. A.; Kielian, M., An Alphavirus E2 Membrane-Proximal Domain Promotes Envelope Protein Lateral Interactions and Virus Budding. *mBio* **2017,** *8* (6).

5. Jose, J.; Przybyla, L.; Edwards, T. J.; Perera, R.; Burgner, J. W., 2nd; Kuhn, R. J., Interactions of the cytoplasmic domain of Sindbis virus E2 with nucleocapsid cores promote alphavirus budding. *J Virol* **2012,** *86* (5), 2585-99.

6. Hartlieb, B.; Weissenhorn, W., Filovirus assembly and budding. *Virology* **2006,** *344* (1), 64-70.

7. Elmasri, Z.; Nasal, B. L.; Jose, J., Alphavirus-Induced Membrane Rearrangements during Replication, Assembly, and Budding. *Pathogens* **2021,** *10* (8).

8. Freed, E. O., HIV-1 assembly, release and maturation. *Nature Reviews Microbiology* **2015,** *13* (8), 484-96.

9. Lingappa, J. R.; Reed, J. C.; Tanaka, M.; Chutiraka, K.; Robinson, B. A., How HIV-1 Gag assembles in cells: Putting together pieces of the puzzle. *Virus Res* **2014,** *193*, 89-107.

10. Sundquist, W. I.; Krausslich, H. G., HIV-1 assembly, budding, and maturation. *Cold Spring Harb Perspect Med* **2012,** *2* (7), a006924.

922 11. Su, Z.; Wu, C.; Shi, L.; Luthra, P.; Pintilie, G. D.; Johnson, B.; Porter, J. R.; Ge, P.;
923 Chen, M.; Liu, G.; Frederick, T. E.; Binning, J. M.; Bowman, G. R.; Zhou, Z. H.; Basler, C. F.;
924 Gross, M. L.; Leung, D. W.; Chiu, W.; Amarasinghe, G. K., Electron Cryo-microscopy Structure
925 of Ebola Virus Nucleoprotein Reveals a Mechanism for Nucleocapsid-like Assembly. *Cell* **2018,**
926 *172* (5), 966-978 e12.
927 12. Wan, W.; Kolesnikova, L.; Clarke, M.; Koehler, A.; Noda, T.; Becker, S.; Briggs, J. A.
928 G., Structure and assembly of the Ebola virus nucleocapsid. *Nature* **2017,** *551* (7680), 394-397.
929 13. Dong, S.; Yang, P.; Li, G.; Liu, B.; Wang, W.; Liu, X.; Xia, B.; Yang, C.; Lou, Z.;
930 Guo, Y.; Rao, Z., Insight into the Ebola virus nucleocapsid assembly mechanism: crystal structure
931 of Ebola virus nucleoprotein core domain at 1.8 A resolution. *Protein Cell* **2015,** *6* (5), 351-62.
932 14. Button, J. M.; Qazi, S. A.; Wang, J. C.; Mukhopadhyay, S., Revisiting an old friend: new
933 findings in alphavirus structure and assembly. *Curr Opin Virol* **2020,** *45*, 25-33.
934 15. Garoff, H.; Simons, K., Location of the spike glycoproteins in the Semliki Forest virus
935 membrane. *PNAS* **1974,** *71* (10), 3988-92.
936 16. Forsell, K.; Xing, L.; Kozlovska, T.; Cheng, R. H.; Garoff, H., Membrane proteins
937 organize a symmetrical virus. *EMBO J* **2000,** *19* (19), 5081-91.
938 17. Lee, S.; Owen, K. E.; Choi, H. K.; Lee, H.; Lu, G.; Wengler, G.; Brown, D. T.;
939 Rossmann, M. G.; Kuhn, R. J., Identification of a protein binding site on the surface of the
940 alphavirus nucleocapsid and its implication in virus assembly. *Structure* **1996,** *4* (5), 531-41.
941 18. Chmielewski, D.; Su, G. C.; Kaelber, J. T.; Pintilie, G. D.; Chen, M.; Jin, J.; Auguste,
942 A. J.; Chiu, W., Cryogenic electron microscopy and tomography reveal imperfect icosahedral
943 symmetry in alphaviruses. *PNAS Nexus* **2024,** *3* (3), pgae102.

944 19. Weaver, S. C.; Winegar, R.; Manger, I. D.; Forrester, N. L., Alphaviruses: population
945 genetics and determinants of emergence. *Antiviral Res* **2012,** *94* (3), 242-57.
946 20. Robinson, M. C., An epidemic of a dengue-like fever in the southern province of
947 Tanganyika. *Cent Afr J Med* **1956,** *2* (11), 394-6.
948 21. Robinson, M. C., An epidemic of virus disease in Southern Province, Tanganyika Territory,
949 in 1952-53. I. Clinical features. *Trans R Soc Trop Med Hyg* **1955,** *49* (1), 28-32.
950 22. Frolov, I.; Frolova, E. I., Molecular Virology of Chikungunya Virus. *Curr Top Microbiol*
951 *Immunol* **2022,** *435*, 1-31.
952 23. Erasmus, J. H.; Auguste, A. J.; Kaelber, J. T.; Luo, H.; Rossi, S. L.; Fenton, K.; Leal,
953 G.; Kim, D. Y.; Chiu, W.; Wang, T.; Frolov, I.; Nasar, F.; Weaver, S. C., A chikungunya fever
954 vaccine utilizing an insect-specific virus platform. *Nat Med* **2017,** *23* (2), 192-199.
955 24. Ganesan, V. K.; Duan, B.; Reid, S. P., Chikungunya Virus: Pathophysiology, Mechanism,
956 and Modeling. *Viruses* **2017,** *9* (12).
957 25. Weaver, S. C.; Lecuit, M., Chikungunya virus and the global spread of a mosquito-borne
958 disease. *N Engl J Med* **2015,** *372* (13), 1231-9.
959 26. Owen, K. E.; Kuhn, R. J., Alphavirus budding is dependent on the interaction between the
960 nucleocapsid and hydrophobic amino acids on the cytoplasmic domain of the E2 envelope
961 glycoprotein. *Virology* **1997,** *230* (2), 187-96.
962 27. Ren, S. C.; Qazi, S. A.; Towell, B.; Wang, J. C.; Mukhopadhyay, S., Mutations at the
963 Alphavirus E1'-E2 Interdimer Interface Have Host-Specific Phenotypes. *J Virol* **2022,** *96* (5),
964 e0214921.
965 28. Suomalainen, M.; Liljestrom, P.; Garoff, H., Spike protein-nucleocapsid interactions drive
966 the budding of alphaviruses. *J Virol* **1992,** *66* (8), 4737-47.

967 29. Lopez, S.; Yao, J. S.; Kuhn, R. J.; Strauss, E. G.; Strauss, J. H., Nucleocapsid-glycoprotein
968 interactions required for assembly of alphaviruses. *J Virol* **1994,** *68* (3), 1316-23.
969 30. Lazaro, G. R.; Mukhopadhyay, S.; Hagan, M. F., Why Enveloped Viruses Need Cores-The
970 Contribution of a Nucleocapsid Core to Viral Budding. *Biophys J* **2018,** *114* (3), 619-630.
971 31. Ribeiro-Filho, H. V.; Coimbra, L. D.; Cassago, A.; Rocha, R. P. F.; Guerra, J.; de Felicio,
972 R.; Carnieli, C. M.; Leme, L.; Padilha, A. C.; Paes Leme, A. F.; Trivella, D. B. B.; Portugal, R.
973 V.; Lopes-de-Oliveira, P. S.; Marques, R. E., Cryo-EM structure of the mature and infective
974 Mayaro virus at 4.4 A resolution reveals features of arthritogenic alphaviruses. *Nature*
975 *communications* **2021,** *12* (1), 3038.
976 32. Skoging, U.; Vihinen, M.; Nilsson, L.; Liljestrom, P., Aromatic interactions define the
977 binding of the alphavirus spike to its nucleocapsid. *Structure* **1996,** *4* (5), 519-29.
978 33. Zhao, H.; Lindqvist, B.; Garoff, H.; von Bonsdorff, C. H.; Liljestrom, P., A tyrosine-based
979 motif in the cytoplasmic domain of the alphavirus envelope protein is essential for budding. *EMBO*
980 *J* **1994,** *13* (18), 4204-11.
981 34. Forsell, K.; Griffiths, G.; Garoff, H., Preformed cytoplasmic nucleocapsids are not
982 necessary for alphavirus budding. *EMBO J* **1996,** *15* (23), 6495-505.
983 35. Brown, R. S.; Wan, J. J.; Kielian, M., The Alphavirus Exit Pathway: What We Know and
984 What We Wish We Knew. *Viruses* **2018,** *10* (2).
985 36. Mendes, A.; Kuhn, R. J., Alphavirus Nucleocapsid Packaging and Assembly. *Viruses* **2018,**
986 *10* (3).
987 37. Kaelber, J. T.; Chmielewski, D.; Chiu, W.; Auguste, A. J., Alphavirus Particles Can
988 Assemble with an Alternate Triangulation Number. *Viruses* **2022,** *14* (12).

989 38. Cheng, F.; Tsvetkova, I. B.; Khuong, Y. L.; Moore, A. W.; Arnold, R. J.; Goicochea, N.
990 L.; Dragnea, B.; Mukhopadhyay, S., The packaging of different cargo into enveloped viral
991 nanoparticles. *Mol Pharm* **2013,** *10* (1), 51-8.
992 39. Cheng, F.; Mukhopadhyay, S., Generating enveloped virus-like particles with in vitro
993 assembled cores. *Virology* **2011,** *413* (2), 153-60.
994 40. Mukhopadhyay, S.; Chipman, P. R.; Hong, E. M.; Kuhn, R. J.; Rossmann, M. G., In vitro-
995 assembled alphavirus core-like particles maintain a structure similar to that of nucleocapsid cores
996 in mature virus. *J Virol* **2002,** *76* (21), 11128-32.
997 41. Colunga-Saucedo, M.; Rubio-Hernandez, E. I.; Coronado-Ipina, M. A.; Rosales-
998 Mendoza, S.; Castillo, C. G.; Comas-Garcia, M., Construction of a Chikungunya Virus, Replicon,
999 and Helper Plasmids for Transfection of Mammalian Cells. *Viruses* **2022,** *15* (1).
1000 42. Li, S.; Zandi, R., Biophysical Modeling of SARS-CoV-2 Assembly: Genome Condensation
1001 and Budding. *Viruses* **2022,** *14* (10).
1002 43. Ruiz-Guillen, M.; Gabev, E.; Quetglas, J. I.; Casales, E.; Ballesteros-Briones, M. C.;
1003 Poutou, J.; Aranda, A.; Martisova, E.; Bezunartea, J.; Ondiviela, M.; Prieto, J.; Hernandez-
1004 Alcoceba, R.; Abrescia, N. G.; Smerdou, C., Capsid-deficient alphaviruses generate propagative
1005 infectious microvesicles at the plasma membrane. *Cell Mol Life Sci* **2016,** *73* (20), 3897-916.
1006 44. Zhang, Y. N.; Deng, C. L.; Li, J. Q.; Li, N.; Zhang, Q. Y.; Ye, H. Q.; Yuan, Z. M.; Zhang,
1007 B., Infectious Chikungunya Virus (CHIKV) with a Complete Capsid Deletion: a New Approach
1008 for a CHIKV Vaccine. *J Virol* **2019,** *93* (15).
1009 45. Li, S.; Tresset, G.; Zandi, R., From disorder to icosahedral symmetry: How conformation-
1010 switching subunits enable RNA virus assembly. *Sci Adv* **2025,** *11* (39), eady7241.

1011 46. Timmermans, S.; Ramezani, A.; Montalvo, T.; Nguyen, M.; van der Schoot, P.; van
1012 Hest, J. C. M.; Zandi, R., The Dynamics of Viruslike Capsid Assembly and Disassembly. *J Am*
1013 *Chem Soc* **2022,** *144* (28), 12608-12612.
1014 47. Li, S.; Erdemci-Tandogan, G.; van der Schoot, P.; Zandi, R., The effect of RNA stiffness
1015 on the self-assembly of virus particles. *J Phys Condens Matter* **2018,** *30* (4), 044002.
1016 48. Cheng, R. H.; Kuhn, R. J.; Olson, N. H.; Rossmann, M. G.; Choi, H. K.; Smith, T. J.;
1017 Baker, T. S., Nucleocapsid and glycoprotein organization in an enveloped virus. *Cell* **1995,** *80* (4),
1018 621-30.
1019 49. Yap, M. L.; Klose, T.; Urakami, A.; Hasan, S. S.; Akahata, W.; Rossmann, M. G.,
1020 Structural studies of Chikungunya virus maturation. *PNAS* **2017,** *114* (52), 13703-13707.
1021 50. Sun, S.; Xiang, Y.; Akahata, W.; Holdaway, H.; Pal, P.; Zhang, X.; Diamond, M. S.;
1022 Nabel, G. J.; Rossmann, M. G., Structural analyses at pseudo atomic resolution of Chikungunya
1023 virus and antibodies show mechanisms of neutralization. *Elife* **2013,** *2*, e00435.
1024 51. Basore, K.; Kim, A. S.; Nelson, C. A.; Zhang, R.; Smith, B. K.; Uranga, C.; Vang, L.;
1025 Cheng, M.; Gross, M. L.; Smith, J.; Diamond, M. S.; Fremont, D. H., Cryo-EM Structure of
1026 Chikungunya Virus in Complex with the Mxra8 Receptor. *Cell* **2019,** *177* (7), 1725-1737 e16.
1027 52. Raju, S.; Adams, L. J.; Earnest, J. T.; Warfield, K.; Vang, L.; Crowe, J. E., Jr.; Fremont,
1028 D. H.; Diamond, M. S., A chikungunya virus-like particle vaccine induces broadly neutralizing
1029 and protective antibodies against alphaviruses in humans. *Sci Transl Med* **2023,** *15* (696),
1030 eade8273.
1031 53. Zhang, Y.; Anbir, S.; McTiernan, J.; Li, S.; Worcester, M.; Mishra, P.; Colvin, M. E.;
1032 Gopinathan, A.; Mohideen, U.; Zandi, R.; Kuhlman, T. E., Synthesis, insertion, and

1033 characterization of SARS-CoV-2 membrane protein within lipid bilayers. *Sci Adv* **2024,** *10* (9),
1034 eadm7030.
1035 54. Panahandeh, S.; Li, S.; Dragnea, B.; Zandi, R., Virus Assembly Pathways Inside a Host
1036 Cell. *ACS Nano* **2022,** *16* (1), 317-327.
1037 55. Panahandeh, S.; Li, S.; Zandi, R., The equilibrium structure of self-assembled protein
1038 nano-cages. *Nanoscale* **2018,** *10* (48), 22802-22809.
1039 56. Zandi, R.; Dragnea, B.; Travesset, A.; Podgornik, R., On virus growth and form. *Physics*
1040 *Reports* **2020,** *847*, 1-102.
1041 57. Liu, H.; Naismith, J. H., An efficient one-step site-directed deletion, insertion, single and
1042 multiple-site plasmid mutagenesis protocol. *BMC Biotechnol* **2008,** *8*, 91.
1043 58. Pierson, T. C.; Diamond, M. S.; Ahmed, A. A.; Valentine, L. E.; Davis, C. W.; Samuel,
1044 M. A.; Hanna, S. L.; Puffer, B. A.; Doms, R. W., An infectious West Nile virus that expresses a
1045 GFP reporter gene. *Virology* **2005,** *334* (1), 28-40.
1046 59. Gadea, G.; Bos, S.; Krejbich-Trotot, P.; Clain, E.; Viranaicken, W.; El-Kalamouni, C.;
1047 Mavingui, P.; Despres, P., A robust method for the rapid generation of recombinant Zika virus
1048 expressing the GFP reporter gene. *Virology* **2016,** *497*, 157-162.
1049 60. Lara-Hernandez, I.; Munoz-Escalante, J. C.; Bernal-Silva, S.; Noyola, D. E.; Wong-
1050 Chew, R. M.; Comas-Garcia, A.; Comas-Garcia, M., Ultrastructural and Functional
1051 Characterization of Mitochondrial Dynamics Induced by Human Respiratory Syncytial Virus
1052 Infection in HEp-2 Cells. *Viruses* **2023,** *15* (7).
1053 61. Rayaprolu, V.; Ramsey, J.; Wang, J. C.; Mukhopadhyay, S., Alphavirus Purification Using
1054 Low-speed Spin Centrifugation. *Bio Protoc* **2018,** *8* (6), e2772.
1055

1056

1057